

The Optical-Near-IR Spectrum of the M87 Jet From HST Observations

Eric S. Perlman ^{1,2,3}, John A. Biretta³, William B. Sparks^{2,3}, F. Duccio Macchetto^{3,4},
and

J. Patrick Leahy ^{3,5}

perlman@jca.umbc.edu

ABSTRACT

We present 1998 HST observations of M87 which yield the first single-epoch optical and radio-optical spectral index image of the jet at 0.15" resolution. We find $\langle \alpha_{ro} \rangle \approx 0.67$, comparable to previous measurements, and $\langle \alpha_o \rangle \approx 0.9$ ($F_\nu \propto \nu^{-\alpha}$), slightly flatter than previous workers. Reasons for this discrepancy are discussed. These observations reveal a large variety of spectral slopes. Bright knots exhibit significantly flatter spectra than interknot regions. The flattest spectra ($\alpha_o \sim 0.5 - 0.6$; comparable to or flatter than α_{ro}) are found in the two inner jet knots (D-East and HST-1) which contain the fastest superluminal components. The flux maximum regions of other knots have $\alpha_o \sim 0.7 - 0.9$.

The maps of α_o and α_{ro} appear poorly correlated. In knots A, B and C, α_o and α_{ro} are essentially anti-correlated with one another. Near the flux maxima of two inner jet knots (HST-1 and F), changes in α_{ro} appear to lag changes in α_o , but in two other knots (D and E), the opposite relationship is observed. This is further evidence that the radio and optical emissions of the M87 jet come from substantially different physical regions. The delays observed in the inner jet are consistent with localized particle acceleration in the knots, with $t_{acc} \ll t_{cool}$ for optically emitting electrons in knots HST-1 and F, and $t_{acc} \sim t_{cool}$ for optically emitting electrons in knots D and E. Synchrotron models fit to the radio-optical data yield $\nu_B \gtrsim 10^{16}$ Hz for knots D, A and B, and somewhat lower values, $\nu_B \sim 10^{15} - 10^{16}$ Hz, in other regions of the jet. If the X-ray emissions from knots A, B and D are co-spatial with the optical and radio emission, we can strongly rule out the "continuous injection" model, which overpredicts the X-ray emissions by large factors. Because of the short lifetimes of X-ray synchrotron emitting particles, the X-ray emission likely traces sites of particle acceleration and fills volumes much smaller than the optical emission regions.

¹Department of Physics, Joint Center for Astrophysics, University of Maryland-Baltimore County, 1000 Hilltop Circle, Baltimore, MD 21250

²Department of Physics and Astronomy, Johns Hopkins University, 3400 North Charles Street, Baltimore, MD 21218

³Space Telescope Science Institute, 3700 San Martin Drive, Baltimore, MD 21218, USA

⁴Affiliated with the Astrophysics Division of the European Space Agency, ESTEC, Noordwijk, Netherlands

⁵University of Manchester, Jodrell Bank Observatory, Macclesfield, Cheshire, SK11 9DL, UK

1. Introduction

The giant elliptical galaxy M87 hosts the best-known extragalactic synchrotron jet. As a result of its proximity (distance = 16 Mpc, Tonry 1991), particularly high resolution studies of its structure are possible (1" = 78 pc). The synchrotron nature of its emissions were first demonstrated by Baade (1956).

Many workers have observed the M87 jet in the radio, optical and X-rays (Perola & Tarenghi 1980; Stocke et al. 1981; Schreier et al. 1982; Smith et al. 1983; Biretta, Owen & Hardee 1983; Killeen et al. 1984; Keel et al. 1988; Perez-Fournon

et al. 1988; Owen, Hardee & Cornwell 1989; Biretta, Stern & Harris 1991, hereafter BSH91; Meisenheimer, Röser & Schlötelburg 1996, hereafter MRS96; Sparks, Biretta & Macchetto 1996, hereafter SBM96; Zhou 1998). Those data have revealed complex structure, with several bright radio-optical knots, as well as significant information on the broadband spectrum of the jet.

The first HST observations of M87 (Boksenberg et al. 1992) revealed considerable detail in the optical jet. Its large scale radio and optical structures are remarkably similar; differences only appear at $\sim 0.1''$ scales (SBM96). More recent HST observations have revealed apparent superluminal motion in several components at speeds up to $6c$ (Biretta et al. 1999; Biretta, Sparks & Macchetto 1999, hereafter BSM99), linking the properties of M87 with those of BL Lacertae objects. HST observations have also served to illuminate the jet's axial structure for the first time, as the radio and optical polarized structures on $0.2''$ scales show strong and consistent differences which indicate that higher-energy particles inhabit regions closer to the jet axis (Perlman et al. 1999, hereafter P99).

The first ground-based multiband, contemporaneous optical photometry of the jet (BSH91) revealed that its spectrum is considerably steeper in the optical than in the radio. More recent ground-based work (MRS96) confirmed this picture, but disagreed with BSH91 on the spectral index of various jet components. Those workers also presented the first detailed fits of synchrotron emission models to broadband, data produced both in their own observations and in those of previous workers (references above) and predicted synchrotron break frequencies $\sim 10^{14} - 10^{15}$ Hz. Pre-COSTAR HST data (SBM96) revealed considerable narrowing of the jet from the radio to the optical, and flatter radio-optical spectra in bright knots. Those workers also extracted optical spectra for large regions of the jet and were the first to fit synchrotron emission models to radio-optical data for the jet at HST resolutions. The model fits indicated stronger magnetic fields, and shorter particle lifetimes in bright knot regions.

Despite this large volume of work, several important questions remain open. For example, the presence of optical synchrotron radiation requires that electrons must be accelerated to at least

$\gamma = 10^6$. Yet the mechanism by which particles are accelerated is poorly known, as are the dynamics of the synchrotron spectrum with time. Moreover, the origin of the X-ray emission from the jet is still not completely constrained (BSH91, Harris et al. 1997, Neumann et al. 1997), and pre-COSTAR HST data were not sufficient to provide a high signal to noise map of the jet's spectral index structure (SBM96).

Here we present 1998 HST observations of the M87 jet, spanning seven bands between $\lambda = 0.3 - 2.05$ microns. These data represent the highest resolution spectral data ever gathered on any extragalactic jet. To analyze the broadband continuum shape, we also include observations taken at 15 GHz with the VLA in 1994. These data allow us to resolve several important issues left unanswered by previous works.

In §2, we will discuss the observational setup and data reduction procedures. Our results will be presented in §3, including both radio-optical and optical spectral index maps of the jet. In §4 we compute synchrotron spectrum fits using our radio-optical data plus X-ray data from the literature. In §5 we compare our results with those of previous authors. In §6 we discuss the physical implications of our results.

2. Observations and Data Reduction

2.1. HST Observations: Design

We imaged the M87 jet with the WFPC2 and NICMOS aboard HST on 25 and 26 February 1998. Data were obtained through six filters, spanning the wavelength range 0.3-1.6 microns. A seventh near-IR band (2.05 microns) was also scheduled for 26 February, but had to be reobserved on 4 April 1998, due to a loss of guide-star lock. In Table 1, we list important details of these observations.

To maximize the observable portion of the jet, the February observations were done with the HST oriented such that the jet fell along a chip diagonal. Unfortunately an equally good orientation was not available on 4 April; as a result, the F205W data do not include the region within $1''$ of the nucleus. In the F110W and F160W bands, the small size of the NIC1 detector made it necessary to observe at two positions. The majority of the observing time for those bands was used on

the inner jet due to its lower surface brightness. To maximize resolution and minimize the effect of known instrumental problems such as grot (Sosey & Bergeron 1999), bad columns and warm pixels, observations in the F205W, F160W, F110W and F814W bands were dithered. We used two-position dithers in F205W, F160W and F110W, while for the F814W observation, we obtained four images in a three-position pattern with sub-pixel dithering. In the F205W band, two dithered 192s observations per orbit were done at a position 700" away to measure the thermal background.

2.2. HST Observations: Data Reduction

We reduced each dataset using the best recommended flatfields, biases, darks and illumination correction images. The IRAF task CRREJ was used to combine CR-split WFPC2 images and eliminate cosmic rays. For the F814W data, we used CRREJ first on the 2 images taken at the central dither position, then shifted the PC images taken at the 2 other positions to be consistent with one another using IMLINTRAN, and then combined those with CRREJ. The product images were then combined using DRIZZLE (Fruchter & Hook 1998, Gonzaga et al. 1998) onto a grid with pixels aligned 45° to the original orientation of the image and smaller by a factor of $\sqrt{2}$. DRIZZLE was also used for the other WFPC images in order to correct for the geometric distortion in the PC chip (Holtzmann et al. 1995), using solutions by Casertano et al. (in prep.)

Unequal pedestal effects in the NICMOS data were eliminated with UNPEDESTAL (van der Marel 1998). No overall pedestal correction was computed, since the signal from the galaxy overwhelms the pedestal. This resulted in only small differences (~ 0.002 ADU/pix/s) near the join of the two point positions used in the F110W and F160W images. In order to minimize color-dependent terms in the NICMOS F110W and F160W flat-fields, we also used color-dependent "superflats" made from long observations of Io (Storrs, Bergeron & Holfeltz 1999). The color dependent terms are reduced significantly in the longer-wavelength bands; moreover, the same concerns are also addressed by the thermal background images taken for the F205W data. The NICMOS images were combined using scripts from the DRIZZLE Handbook (Gonzaga et al. 1998)

and offsets computed from the *jitter* files using the script BEARING by E. Bergeron (mentioned in Gonzaga et al.). To correct for geometric distortion and the slightly rectangular pixels, we used solutions by Cox et al. (1997). Thermal background images for the F205W band were combined in the same way and then subtracted.

Galaxy subtraction was done using the tasks ELLIPSE, BMODEL and IMCALC. To successfully model the galaxy, we masked out the jet and SW hotspot, as well as all globular clusters and stars. This is of necessity an iterative process, as the fainter globular clusters do not become apparent until galaxy subtraction is done. Failure to mask a globular cluster would produce a circular "ringing" at the distance of the cluster. In the WFPC2 images, we only fit a galaxy model to the data on the PC chip, in order to minimize the effect of the chip join, which was found to produce a circular "ringing" near the radius of knot F in fits done with the entire 4-chip WFPC2 mosaic. Due to the faintness of the galaxy in the UV, we were only able to subtract the galaxy from the F300W image after smoothing it with a Gaussian. In the NICMOS mosaics, it was necessary to manually mask out regions where no data exists. The smallness of the NIC1 chip only made it possible to model the galaxy in the F110W and F160W images to a distance of $\sim 19''$ from the nucleus. This also necessitated an iterative approach to finding the correct ellipticity and PA of the model galaxy in the F110W and F160W bands (*n.b.*, it was not possible to assume a surface brightness model derived from the WFPC2 images and scaled to the nuclear flux because of significant large-scale color gradients within the galaxy itself). Subsequent testing revealed that in all bands we were able to achieve residuals no larger than a few ADU/pix, with no large-scale trends which might indicate incorrect ellipticity or "ringing" in most regions, although there are significant dust known lanes in the inner galaxy (Sparks et al. 1993). The dust lanes affect only one region of the jet, knot HST-1. RMS errors from the galaxy subtraction are included in our error estimates in each case by adding in quadrature.

Flux calibrated images were obtained by multiplying the reduced and galaxy-subtracted image by using the task CALCPHOT in SYNPHOT. We used CALCPHOT to do this task rather than the

information in the headers because it allowed us to assume a spectral index value (we used $\alpha = 0.9$, which is close to the mean spectral index of the jet) and thus refine the flux calibration⁶ of the PHOT-FLAM value from SYNPHOT. This also allowed us to apply a decontamination correction (Baggett et al. 1997, Baggett & Gonzaga 1998), which affected most bands by $\lesssim 3\%$, but had a larger effect on the F300W data (8%). To simulate the size of the aperture correction due to the extreme wings of the PSF, we used the knot A+B+C region and a TinyTim PSF for the F205W+NIC2 combination. Those simulations led us to adopt an aperture correction of 1.107 for regions which extend $\sim 1''$ (on each side) beyond regions of the jet with *visible* flux (such simulations are recommended for estimating the aperture correction for extended sources; see NICMOS team 1999). Conversion from F_λ to F_ν was done at each band's pivot wavelength (λ_{eff} in Table 1).

Considerable effort was expended to estimate the uncertainties in these data. Several possible sources of error were accounted for, including zeropoint errors in the SYNPHOT calibration (Colina et al. 1998 for NICMOS; Baggett & Gonzaga 1998, Baggett et al. 1997 and Whitmore & Heyer 1995 for WFPC2; typically this error is $\lesssim 3\%$), possible errors due to assuming the wrong slope for the jet in SYNPHOT (at most 1-2%, even if standard SYNPHOT coefficients instead of ones calculated for $\alpha = 0.9$ are used), flatfielding errors ($\lesssim 2\%$ for WFPC2, Whitmore & Heyer 1997, but $\sim 3 - 5\%$ for NICMOS, Calzetti & Gilmore 1998) and Poisson errors both in the data and in the subtraction of the galaxy (see above). These errors have been propagated by adding in quadrature.

Once these steps were done, all images were rotated so that the jet was along the x axis (the centerline of the jet was assumed to lie at PA 290.5°), using the positional and orientation information in the headers. Images were then convolved with Gaussians so that their resolution (FWHM) was equal to that of the F205W image (TinyTim PSFs were not used because of the large number of bands and difficulties associated with deconvolution tasks). We then resampled all images to the

⁶note that the differences between the values derived for $\alpha = 0.9$ and the values in the headers were in all cases $< 3\%$

nominal NIC2 pixel size of $0.0758667''/\text{pix}$ and placed them on identical coordinate grids, with the nucleus at (20,200) on 400×400 pixel images. Testing has revealed that the alignment of these images is accurate to within 0.15 pixels. The resolution of the spectral index maps we show in §§3 and 4 is therefore $\sim 0.15''$ FWHM, translating to 12 pc at the distance of M87.

2.3. VLA Data

To analyze the jet's broadband spectrum, we include previously published radio data (Zhou 1998, P99), obtained in February 1994 at 15 GHz. The data reduction procedures for this dataset have been described in Zhou (1998) and P99. To facilitate direct comparison between the radio and optical images, the radio image was resampled and shifted to the same frame of reference and pixel scale as the HST images (see above).

While the radio data were obtained in February 1994, the possible effect of variability is small. Even for the largest radio variability found between 1993 and 1997 ($\sim 40\%$ for HST-1; Zhou 1998), the effect on α_{ro} is only $\Delta\alpha_{ro} = 0.04$. The resolution of the radio and F205W images is very similar ($0.14''$ FWHM compared to $0.15''$ FWHM) so we did not have to convolve the radio image with a Gaussian before comparisons were done, and we were able to use the same aperture correction.

3. Radio-Optical and Optical Continuum Shape

In Figure 1, we show the WFPC2 300W and F814W images, and the F160W NICMOS image, all at full resolution. The structures seen in the three bands are similar, indicating that spectral curvature exists in various jet components tend to be gradual. We examined the profiles on each HST image of slices through resolved areas of the jet. These comparisons were done on convolved data only, to exclude resolution effects. We confirm the result of SBM96 that the jet is narrower in the optical than the radio. However, based on our data there is no evidence that significant narrowing takes place in the optical.

3.1. Spectral Index Fits

We generated optical and radio-optical spectral index maps (α_o and α_{ro} ; $F_\nu \propto \nu^{-\alpha}$), using simple weighted least-squares fitting algorithms in IDL. In Figure 2a, we show the optical spectral index map. Both the α_o and α_{ro} images were clipped in regions where the signal to noise in either the F814W or radio image was less than 4. In Figure 2b, we show the radio-optical spectral index (α_{ro}) map. The same figure also shows maps of synchrotron model fit parameters in panels 2c and 2d (see §4 for description of those and discussion). The convolved F814W image is shown for comparison in Figure 2e.

The lack of “ringing” near compact features in the α_o map indicates that the differing resolutions in the HST images were correctly accounted for, and also that the registration is quite good. There is a large steep-spectrum region at the southern end of the A+B+C complex, but it is clearly real since (1) there is no corresponding feature near the southern end of the inner jet, and (2) there is more flux and extent to the south of the bright regions in A+B+C than to the north (see the images in SBM96 and P99 as well as Figure 1).

In Figure 3, we show runs of α_o , α_{ro} , $\alpha_o - \alpha_{ro}$ and flux with distance along the axis of the jet in the inner jet (0 – 10'' from the nucleus). Figure 4 shows the same plots for the outer jet (10 – 20'' from the nucleus). The spectral indices given in those figures are flux-weighted on a row-by-row basis, with flux summed in a 1.5'' wide window for Figure 3 and a 6'' wide window for Figure 4.

We also extracted fluxes for each knot (and some sub-knot regions) in the jet. These points are listed in Table 2, and plotted along with the best-fit power laws in Figure 5. As can be seen, the single power law model is a good fit for most regions, although a few show signs of gradual curvature in the optical. Table 2 also defines the regions used for each knot. We also applied an aperture correction of 1.107 (§2.2) to both the radio and optical data.

3.2. Overall Spectral Morphology

In the optical, all knots in the jet are well fit by single power laws. Evidence for spectral curvature in the optical can, however, be seen in D-E, D-M, A shock, B-1, B-2 and C (Fig. 5). In all

of these cases the curvature appears to be very gradual and in the sense of spectral steepening towards the blue, as expected in all standard models of synchrotron emission (see §4).

The jet average is $\langle \alpha_o \rangle \approx 0.9$, slightly flatter than reported in MRS96 ($\langle \alpha_o \rangle \approx 1$), but significantly flatter than reported in BSH91 and SBM96 ($\langle \alpha_o \rangle \sim 1.3$). We will examine possible reasons for this in §5. We derive $\langle \alpha_{ro} \rangle \approx 0.67$, very similar to values observed by previous workers (BSH91, MRS96, SBM96).

Bright regions of the knots have somewhat flatter optical spectra than other regions of the jet, with $\alpha_o \sim 0.5 - 0.8$ near flux maxima, and substantial steepening to $\alpha_o \sim 0.8 - 1$ immediately downstream. Two regions are particularly flat ($\alpha_o \sim 0.5 - 0.6$): the flux maxima of knots HST-1 and D-East. Regions near the flux maxima in E, I and A have only slightly steeper spectra ($\alpha_o \sim 0.6 - 0.7$). By comparison, the inter-knot regions show significantly steeper optical spectra ($\alpha_o \sim 1.0 - 1.2$), although our signal to noise in those regions is somewhat low and our errors are correspondingly larger.

Much smaller variations are observed in α_{ro} than α_o . Slightly steeper values ($\alpha_{ro} \approx 0.70$) are seen in most regions of the inner jet (interior to knot A), with slightly flatter values ($\alpha_{ro} \approx 0.66$) observed near the flux maxima of knots HST-1, D-East, E and F. By contrast, in the outer jet, a very different pattern is observed: α_{ro} is remarkably stable, varying by at most ± 0.03 , with no apparent correlation between jet flux and α_{ro} .

In most regions of the jet, the optical spectrum is somewhat steeper than the radio-optical continuum. This can be seen on Figures 3c and 4c, where runs of $\alpha_o - \alpha_{ro}$ are plotted. Values of $\alpha_o - \alpha_{ro}$ average ~ 0.1 in bright regions in the inner jet, and ~ 0.2 in the outer jet. The flux maximum regions of HST-1, D-East, E, I and A, show no evidence of radio-optical curvature (in fact at their flux maxima HST-1 and D have α_o somewhat flatter than α_{ro} , but at only the 2σ level). Significantly larger values of $\alpha_{ro} - \alpha_o$ are observed downstream of the flux maxima in each knot, indicating increased curvature. Interestingly, we observe a nearly constant value of $\alpha_o - \alpha_{ro}$ in knot regions outside of flux maxima, with no trend for increasing curvature as the distance from a local maximum increases.

Perhaps the most glaring feature seen in Figures 2 and 4 is the oscillation of spectral indices, and the overall anti-correlation of α_o and α_{ro} , observed in the outer jet. As can be seen, the α_o and F_I maps track each other quite well but appear almost anticorrelated with α_{ro} , in the sense that the flattest α_o points also represent the brightest points, but those same points have the steepest values of α_{ro} .

The above discussion indicates that the spectral morphology of the M87 jet is highly complex. It is worthwhile to discuss the jet's spectral morphology and the relationship of the optical and radio spectral indices in greater detail, isolating each jet region in turn. The implications of various features of the jet's spectral morphology will be discussed in §6.

3.3. Spectral Morphology: Inner Jet

We turn first to the inner jet, which has a knotty morphology, dominated by five discrete regions. Proceeding outwards, the first knot is HST-1, $1''$ from the nucleus. At $0.15''$ resolution, HST-1 consists of a bright peak with fainter regions downstream. At higher resolution it breaks up into several components, which appear to move at speeds up to $6c$ (Biretta et al. 1999, BSM99). Near the optical flux peak are local minima in both α_o and α_{ro} , but the beginning of the flat α_o region appears to be $0.15''$ upstream from the beginning of the flat α_{ro} region. Given the proximity to the central nuclear source and the location of a nearby dust lane, this result should be confirmed in future studies.

The brightest knot in the inner jet is knot D, located $2.5 - 4''$ from the nucleus. Knot D can be separated into three regions: the flux maximum, called D-East, the southern 'twist', called D-Middle, and the western edge, called D-West. Within this knot are superluminal components moving at speeds ranging from $2 - 5c$ seen in both the optical (Biretta et al. 1999a, BSM99) and radio (Biretta et al. 1995). The α_o map tracks closely the distribution of optical flux all throughout knot D, with the flattest spectral indices observed in a compact ($\sim 0.4''$) region at the flux maximum. Less prominent local minima, are seen near the flux maxima in D-Middle and D-West. The distribution of α_{ro} is somewhat different: the minimum in α_{ro} occurs $0.15''$ upstream of the ex-

trema in α_o and F_I ; the increase in α_o which follows the flux maximum also appears to lag the increase in α_{ro} by this same amount. These two features show up most dramatically in the run of $\alpha_o - \alpha_{ro}$ (Fig. 3c). The α_{ro} image does not show significant local extrema near the locations of either D-Middle or D-West, but some slight flattening trend is seen over this region. Regions closer to the jet axis appear to have flatter values of α_o than the northern or southern edges, but this is not at all clear for α_{ro} .

At about $6''$ from the nucleus we observe knot E, which is barely resolved along the jet axis at $0.15''$ resolution (at higher resolution two condensations are seen; SBM96). Speeds of $\sim 3.5c$ have been detected in our HST monitoring program (BSM99). Knot E does not exhibit the sharp spectral changes seen in knot D, but nevertheless a flatter- α_o region is seen centered roughly on the flux maximum. There is also a local flattening in α_{ro} which appears more extended along the jet axis than the flat- α_o region; however α_{ro} reaches minimum $0.25''$ upstream of α_o . Unlike in knot D, however, the downstream ends of the flat α_o and α_{ro} regions appear spatially coincident.

Knot F, located $8 - 9''$ from the nucleus, appears rather amorphous at $0.15''$ resolution but breaks up into two diffuse blobs at higher resolution. Radio monitoring has detected speeds near c in this region (Biretta et al. 1995), but our optical monitoring has not yet detected proper motion (BSM99). Knot F's spectral morphology appears rather subtle (Figures 2a-b, 3). Both the α_o and α_{ro} images show flatter spectral indices closer to the jet axis than along the northern or southern axes. Neither spectral index map shows strong local extrema, but instead both show a flat spectrum region roughly coincident with the rather broad flux maximum region. At its upstream end, α_{ro} appears to lag α_o by $0.17''$, but the situation is reversed at the downstream end, where the flat α_o region terminates $0.2''$ before the termination of the flat α_{ro} region.

Knot I, located $11''$ from the nucleus, appears to have motions near c from HST monitoring (BSM99). Examination of Figures 2a and 2e reveals a fairly compact flat- α_o region centered on the flux maximum. However, the changes in α_{ro} are not well localized to the flux maximum region.

3.4. Spectral Morphology: Outer Jet

As has been noted by many authors, the morphology of the outer jet is quite different from that of the inner jet. The outer jet features four knot complexes, traditionally called A (12 – 14" from the nucleus), B (14 – 16" from the nucleus; *n.b.* neither the downstream end of knot A nor the upstream end of knot B has a sharp “edge”), C (17 – 19" from the nucleus) and G (> 19" from the nucleus).

Looking at the outer jet in Figures 2a-b and 4, one is immediately struck by the strong anti-correlation between α_o and α_{ro} . This anti-correlation begins in the inter-knot region between I and A, 11.4 – 11.8" from the nucleus, where we observe a flattening in α_{ro} with a possibly double structure, corresponding to a region with steep α_o . Further downstream, the flux maxima in A, B and C all correspond to regions with flat α_o but steep α_{ro} values, as do the ‘filamentary’ structures in this region (although the departures are smaller than for the flux maxima). Also agreeing with this trend are the steeper than average values of α_o and flatter than average values of α_{ro} seen in the B-C interknot region. A close look at Figures 2a-b and 4, in fact, reveals, that local minima in α_o coincide very closely with local maxima in α_{ro} and vice versa; moreover the locations of increases in α_o also coincide very closely with decreases in α_{ro} and vice versa.

4. Synchrotron Spectrum Models

We fitted synchrotron spectrum models to the integrated radio through X-ray fluxes for knots A, B and D as well as the larger A+B+C complex, and on a pixel to pixel basis to radio through optical data for the entire jet, using programs written by C. Carilli and J. P. Leahy (Carilli et al. 1991, Leahy 1991). In these fits we include X-ray data in our analysis for comparison with the total fluxes of knots A, B and D, where X-ray emissions have been detected (Schreier et al. 1982, BSH91). For knot A, we use X-ray fluxes from a January 1998 ROSAT HRI observation (Harris et al. 1998). For knots B and D, fluxes have not yet been extracted from ROSAT data, so we used

1 keV fluxes from *Einstein* (BSH91)⁷. The conversion of X-ray counts to flux for all regions was done assuming $\alpha_x = 1.3$ and $\log N(H) = 20.38$ (BSH91). Even though the X-ray data for B and D are not contemporaneous, this will have only a small effect on α_{ox} . A 50% change in flux (3× as large as the variations in A documented by Harris et al. 1997, 1998) would only produce a change of $\Delta\alpha_{ox} = 0.10$.

The models we fit were:

(1) A Jaffe & Perola (1973) model (hereafter JP), which allows for continuous isotropization of the pitch-angle distribution of the electron population with time, but no further particle injection.

(2) A Kardashev-Pacholczyk model (Kardashev 1962, Pacholczyk 1970; hereafter KP), which does not allow pitch-angle scattering, and therefore allows the development of a high-energy “tail” of particles at oblique pitch angles.

(3) A “continuous injection” (hereafter CI) model (Heavens & Meisenheimer 1987, Meisenheimer et al. 1989) under which a power-law distribution of relativistic electrons is continuously injected. This model was originally developed for the case of an unresolved source. Meisenheimer et al. (1989) and Heavens & Meisenheimer (1987) have shown that this model applies when there exists within the telescope beam an unresolved zone of continuous high-energy particle injection (*e.g.*, a shock front).

Each model can be characterized by an injection index α_{in} and a break frequency ν_b . The differences between the JP, KP and CI spectrum show up most strongly blueward of the break. The JP spectrum has the fastest cutoff, the CI spectrum has the least steep break, and the KP model’s cutoff is intermediate between the two. Importantly, the overall trends fit by each model are identical (*e.g.*, if a region has high ν_b , this will be true under all three models). Therefore, the pixel-by-pixel fits were done assuming only the KP model.

In fitting integrated fluxes, we tried only $\alpha_{in} = \alpha_{ro}$, as well as $\alpha_{in} = \langle \alpha_{in} \rangle$ (with the mean derived from the α_{in} map). We did not attempt a χ^2 minimization for these fits because all of those models

⁷Recent observations of the M87 jet by *Chandra* have in fact detected X-ray emission from all knots in the jet (Marshall et al. 2001).

have relatively fixed general characteristics; moreover, as we will emphasize, because of the large gaps which exist in the mid to far IR as well as UV, there are significant limits to what this procedure can do. The results of these fits are shown in Figures 6a-e, and the derived ν_b , α_{in} and χ^2 values are summarized in Table 3.

Inspection of Figure 6 reveals a striking result: independent of whether the X-ray emissions are synchrotron in nature, the CI model is decisively ruled out by our data because it overpredicts by large factors (5-50) the X-ray fluxes. The CI spectrum could be made to work for knot A if the X-ray emitting electrons occupy a region about 1/5 the volume of knot A in the optical, but greater reductions are necessary for knots D (factor 8) and B (factor 50). This topic will be discussed further in §6.

By comparison, both the JP and KP models fit the data reasonably well; our data cannot discriminate between these models because there are no data in the break region (the EUV). An interesting point in favor of a synchrotron nature for the X-ray emissions is that in knot D, JP and KP models fit to only the radio through optical data, predict the X-ray emissions to within a factor ~ 2 .

Pixel by pixel fits were done only to the radio through optical data. In Figures 2c and 2d, we show (respectively) maps of ν_b and α_{in} for the KP model only. Note that good quality fits were only achieved in knot regions and so we have clipped these images so that they do not include interknot regions. For Figure 2c, the color scale runs from $10^{14.5}$ to 10^{16} Hz, while the color scale for Figure 2d is identical to that used for Figure 2b.

We derive break frequencies $\sim 10^{16}$ Hz in most inner jet regions. Note that values $\sim 10^{16}$ Hz should be treated as guidelines and/or lower limits. Due to the gradual curvature of synchrotron spectra (*e.g.*, Figure 6), a lack of significant radio-optical curvature makes fitting values of α_{in} and ν_b difficult, and in such cases the code used outputs ν_b values 10 times higher than the highest frequency for which data are present (here 10¹⁵ Hz). Somewhat lower break frequencies ($3 - 10 \times 10^{15}$ Hz) were found in knots A, B and C, with higher break frequencies in flat-spectrum regions near knot maxima. Note that we do not quote break frequencies in inter-knot regions because the fits in those regions were poor due to their low signal

to noise. These values agree well with those we find for the integrated fluxes of knots D, A and B, but with the addition of X-ray data.

The ν_b (Figure 2c) and α_o (Figure 2a) maps are extremely well correlated, with high break frequencies in the flattest spectrum regions, and low break frequencies in the fainter, steep spectrum regions. Also, the α_{in} map (Figure 2d) largely correlates with the α_{ro} map (Figure 2b). Both of these are to be expected given the rather large gap (4 decades in frequency) between the radio and optical points. Note that also from a physical point of view one expects α_{ro} and α_{in} to be correlated unless there is significant low-frequency radio structure which is self-absorbed by 15 GHz. We do not have the data to test for this possibility but it is somewhat beyond the scope of this paper.

5. Comparison With Previous Work

We report average values of α_{ro} which are comparable to those reported by other authors. The average value of α_o we find (0.9) is, however, flatter than values reported by previous authors, which range from $\langle \alpha_o \rangle \approx 1.0$ (MRS96) to $\langle \alpha_o \rangle \approx 1.3$ (BSH91 and SBM96). It is worthwhile to look at the likely reasons behind these discrepancies. Since the regions used to obtain fluxes (as well as the calibration process) varied in each case, the comparison is somewhat difficult. We therefore will speak in rather broad terms about the global picture, and concentrate on the A+B+C region, for which all previous workers except for SBM96 have compiled fluxes, summarized in MRS96.

As already mentioned, Figures 6d and 6e contain our fluxes for the knot A+B+C region as well as the synchrotron spectrum fits for this region. We have overplotted on Figures 6d-e the other fluxes quoted by MRS96; particularly relevant to this discussion is Figure 6e which zooms in on the optical. As can be seen, our flux values are well in accord with all but two teams' fluxes. The discrepant values are from BSH91 and Killeen et al. (1984). We cannot throw any additional light on why those values are discrepant; we refer the reader to the discussion in MRS96 on this point. Moreover, the overall value of spectral index one derives from our values is easily seen to be identical within the errors to what one would derive from all previous points except the IUE values (Per-

ola & Tarenghi 1980), which may be discrepant because of poor galaxy subtraction. Those values bear some mention as they account for most of the curvature in the models fit by MRS96 to the data for A+B+C, and also have by far the largest error bars. Also, those points, plus those of BSH91, are the only ones consistent with a steep value for α_o in the A+B+C region.

As can be seen by comparing our Figures 3a and 4a with Figure 3 of MRS96, our values and those of MRS96 for α_o are completely consistent if a constant offset of $\Delta\alpha_o \approx 0.1$ is applied, and fine structure on scales smaller than an arcsecond is ignored. It is likely that the main reason for the constant offset is contamination from the galaxy, which would tend to redden the spectrum, since the mean color of starlight from M87 is significantly redder than the jet ($R - I$ color of the galaxy's light averages 0.78 mag, Boroson & Thompson 1991; as compared to $r - i = 0.16$ mag for knot A of the jet, BSH91). This is perhaps not entirely unexpected given the much higher resolution of HST compared to ground-based telescopes. It is hard to imagine other significant color-based or systematic effects given that the overall flux scales agree quite well (Figure 6e). A second factor in this respect, however, could be the larger number of bands in our data set (7 compared to 3) which allows us to better fit spectral indices as well as see curvature.

We fit models which are somewhat different than those fit by MRS96. In particular we do not make assumptions about the nature of a spectral cutoff at high frequencies. Therefore it is somewhat confusing to compare the values of *break* frequency we derive to the values of *cutoff* frequency they derive. It is also important to note that the comment made in MRS96 that there is evidence for a steeper cutoff than predicted by Fermi acceleration was based only on the IUE points and so this needs to be verified (we have since obtained shorter wavelength data with STIS; those data will be the subject of a later paper). Given all of this plus the somewhat flatter values of α_o we find, it is therefore not surprising that our values for ν_b are higher than their ν_{cutoff} values. In comparing the two tracks however (cf. Figure 8b in MRS96 and our Figure 2c) it is important to note that, particularly in the outer jet, the overall trends are exactly the same except for the resolution differ-

ence.

The values reported by SBM96 were based on pre-COSTAR HST data. A significant number of those datasets are low S/N and the spectral index fits in SBM96 were not weighted by signal to noise. Moreover, the regions used by SBM96 contain large non-jet portions because they were rectangular regions defined on an image where the jet was inclined by roughly 21° to the x axis. The data used here are considerably higher signal to noise in every band, and the jet is on the x axis; in addition, we do not have to deal with the residuals caused by deconvolving the pre-COSTAR PSF in each band. We have refit spectral indices to the quoted flux values for various jet regions, using only the F140W, F220W and F372M datasets (the only ones with reasonably good S/N over large parts of the jet). When this is done we obtain optical spectral indices considerably flatter than those obtained by SBM96 (probably due to our exclusion of the lower signal to noise data, which also would have had poorer galaxy subtraction), and indeed in bright regions such as knot A we obtain results comparable to within the errors. We have also resampled those images to $0.0758667''/\text{pix}$, smoothed them to $0.15''$ resolution, and fit a spectral index image using the same program described in §3. The result is extremely noisy (with error bars much larger than in our data), but spectral indices considerably flatter than 1 are found in bright regions; in fact near the flux maxima of A and D-East spectral indices $\sim 0.4 - 0.7$ are found, with internal error bars $\sim \pm 0.2$. This tends to support the reliability of our results.

Finally, there is also a large discrepancy between our spectral index values and those quoted by BSH91. As we have already commented (and as previously noted by MRS96), however, the flux scale used in BSH91 appears to be rather at variance with that of other workers. We do not have significant new light to throw on the flux scale issue but given the overall good agreement of our flux scale with that of previous workers we are suspicious of the spectral index values quoted by BSH91.

6. Discussion

We have presented data which give the first high-resolution picture of the near-infrared to ul-

traviolet spectrum of the M87 jet, and indeed represent the first dataset of this type for any extragalactic jet. We have given a detailed discussion of the spectral morphology of the jet and the $\alpha_o - \alpha_{ro}$ relationship in §§3.3 and 3.4, and discussed synchrotron spectrum model fits in §4. These allow us to place significant constraints on the jet structure, the nature of the X-ray emission, and also the extent, need and nature of particle acceleration in the M87 jet. We discuss each of these topics in turn.

6.1. Nature of the X-ray Emission

Our data are fully consistent with a synchrotron origin for the X-ray emission in the jet (as proposed by BSH91). The observation of variability in the X-ray emission from knot A and the nucleus (Harris et al. 1997, 1998), rules out a thermal bremsstrahlung nature for the X-ray emission. But neither our data nor the observed variability are completely sufficient to rule out an inverse-Compton nature for the X-ray emission.

If one assumes that the X-ray, optical and radio synchrotron emitting electrons in knots A, B and D are co-spatial, the CI model of Meisenheimer et al. (1989) is ruled out because it overpredicts by large factors the observed X-ray emission. Thus particle injection or acceleration can occur only in discrete sites occupying a small fraction of the jet volume. This agrees with the compactness required by the detection of X-ray variability in knot A on timescales of months (Harris et al. 1997, 1998). The CI model can be made to work for knot A if the X-ray emitting electrons in that knot occupy a region about 1/5 the projected area of knot A in the optical. Similar arguments can be made for knots D (factor 8) and B (factor 50), although their X-ray detections are less secure.

Measurement of the X-ray spectral index α_x would allow us to discriminate between the synchrotron and inverse-Compton models. Inverse-Compton X-ray emission would have a much flatter X-ray slope ($\alpha_x \sim 0.7$, comparable to the jet's α_{ro} and similar to the average hard X-ray slopes of low-energy peaked BL Lacs (LBL) found by ASCA, see Kubo et al. 1997), than both the JP and KP synchrotron models, which predict $\alpha_x \sim 1.5 - 2$ and $\alpha_{ox} < \alpha_x$, as seen in the X-ray spectra of most high-energy peaked BL Lacs (HBL; Perlman et al. 1996, Sambruna et al.

1996).

Unfortunately, because of the multi-component nature of the X-ray emission from the M87 region (including cluster, galaxy and jet components), current X-ray data do not allow us to place good limits on the shape of the X-ray slope of M87's jet. This could not be done from the *Einstein* HRI or ROSAT HRI datasets due to their poor (at most two-channel) energy resolution. Higher energy telescopes (ASCA, SAX and RXTE) have tried to determine the relative jet+nuclear X-ray emissions but with at best variable success due to their much poorer ($\sim 1 - 3'$) angular resolution. Matsumoto et al. (1996) and Allen et al. (2000) both find some evidence of a hard X-ray tail in ASCA data but with large error bars on the spectral shape ($\alpha = 0.4^{+0.4}_{-0.5}$ between 2-10 keV). Similar constraints ($\alpha_x = 0 \pm 1$), have recently been obtained from SAX data (Guainazzi & Molendi 1999). However, a negative detection was obtained by RXTE (Reynolds et al. 1999), a non-imaging detector, which places a lower limit of $\alpha_x = 0.7$ on the spectral index of knot A, and $\alpha_x = 0.9$ on the core. Comparison of the fluxes obtained in the two detections plus the upper limits, however, does reveal evidence of variability (Guainazzi & Molendi 1999, Reynolds et al. 1999). Thus current X-ray data cannot constrain the spectral shape of any component in the M87 jet, but they do constrain the nature of the emission to non-thermal (synchrotron or inverse-Compton) mechanisms because of the observed variability.

6.2. Jet Structure

As shown in Figures 2-4 and §3, the relationship between α_o and α_{ro} in the M87 jet is rather complex. In the inner jet, the two appear correlated in most regions if a lag is applied to one or the other, while they are essentially anti-correlated in the outer jet. These trends are further evidence that it is impossible to model the M87 jet as an axially homogeneous jet where radio and optical synchrotron emitting electrons are completely co-spatial. Instead, they support a model for the structure of the jet presented by P99, whereby the energy spectrum of electrons in the jet, and magnetic field direction, vary significantly with distance from the jet axis. In the P99 model, higher-energy electrons are concentrated closer to the jet axis, where the magnetic

field is most strongly affected by shocks and other disturbances, while lower-energy electrons occupy mainly the jet “sheath” at greater distances from the jet axis. At any one point, the observed spectral indices include both core and sheath contributions, with the core dominating in the optical and the sheath dominating in the radio. This model predicts that α_o and α_{ro} should not vary together. It also predicts that some regions might have flatter *observed* values of α_o than α_{ro} , since different regions can predominate in different bands. This is in fact observed at the flux maxima of HST-1 and D.

The poor correlation between α_o and α_{ro} in the outer jet is somewhat more surprising given the large degree of similarity between the radio and optical polarized structure in this region (P99). However, in the absence of strong shocks it is still entirely possible for energy stratification to occur without observing significant differences in polarimetry. Indeed, we should point out that the mixing of previously stratified layers would not be expected to occur in a short, linear shock, and would likely produce turbulence which would be visible in the form of eddies (not observed). Moreover, the optical polarized structure of the outer jet, while much more similar to that seen in the radio, still does show evidence that shocks begin in the jet interior, particularly in the pre-shock regions of A and C (refer to Figures 2, 5 and 6 of P99). The details of the spectral index maps we find indicate that regions of the jet closer to the axis probably have somewhat steeper values of α_{ro} and hence α_{in} , than the sheath.

The finding that the X-ray emissions must fill a volume significantly smaller than the lower-energy emission also agrees with the stratification proposed by P99. It should be noted that because of the observed variability, this result is independent of whether the X-ray emission mechanism is synchrotron or inverse-Compton.

6.3. Is *In Situ* Particle Acceleration Necessary?

The issue of whether *in situ* particle acceleration is required for the M87 jet, is complex and not well explored. As explained by BSH91, particle acceleration is required if the magnetic field is near the equipartition value of $B \sim 200\mu\text{G}$. This is underlined by our data, which yield “syn-

chrotron ages” for knots D, A and B of 60-100 years under the JP model, and somewhat higher (110-280 years) under the KP model, similar to values calculated by BSH91 under different assumptions. However, the radiative lifetimes of synchrotron emitting particles vary strongly with magnetic field ($\propto B^{-3/2}$), so that if the magnetic field is significantly weaker than the equipartition value (Heinz & Begelman 1997), it is not unfeasible to reconcile the radiative lifetimes of synchrotron emitting electrons with the length of the jet (~ 2 kpc).

The local variations in optical spectral index and break frequency we find, as well as the optical, radio and X-ray variability observed in HST-1, D and A (Biretta et al. 1999, Zhou 1998, Harris et al. 1997, 1998), represent strong evidence for particle acceleration near the flux maxima of those regions. Such particle acceleration is in fact expected if knots D and HST-1, where several variable superluminal components have been found in both HST and VLA monitoring, are analogous to flaring regions in blazar jets. Moreover, the details of the optical polarimetry in those and other regions (P99), where we observe magnetic field vectors to be strongly compressed transverse to the jet direction, creates all the conditions necessary for particle acceleration.

If indeed the observed changes in spectral index are a product of particle acceleration, then Figures 3-4 represent a time history of particle acceleration and synchrotron aging in the jet in regions where the implied lag $<$ light-crossing time of the jet. This interpretation allows us to comment on the nature of particle acceleration in the M87 jet, as well as the acceleration and cooling timescales, because it transforms the observed differences in the runs of α_o and α_{ro} versus distance into time lag information. In two knot regions it appears that variations in α_o lag variations in α_{ro} . In D-East, a lag of $0.15''$ is observed, which translates to about 7.5 years using the observed speeds $\sim 5c$ in this region (BSM99). The somewhat larger lag of $0.25''$ seen in knot E translates to about 14 years given the speeds in BSM99. There are also two knot regions (HST-1 and F) where we observe the opposite trend: α_o leading α_{ro} . In the case of knot HST-1 the observed lag translates into a period of ~ 7 years given the speeds in BSM99 (greater precision is not possible given the nearness of the

point source), while for knot F we cannot translate the lags into timescales directly since the velocity fields are not well known in those knots.

If particle acceleration is present in the M87 jet, the mechanism is not well constrained. Several mechanisms have been proposed, including magnetic reconnection (Lesch & Birk 1999) and Fermi acceleration in knots (Meisenheimer, Yates & Röser 1997). The structure of the jet, which contains many shock-like, flat-spectrum knots (see also P99), argues against a major role for magnetic reconnection. In contrast, the observation of sharp changes in optical magnetic field position angle in these same flat-spectrum knots (P99), suggests compression of the magnetic field in the jet interior at these positions, more consistent with shocks.

The observed spectral variations near knot maxima in the inner jet are consistent with models for flares produced by shock-induced particle acceleration. As Kirk, Rieger & Mastichiadis (1998) have shown, the evolution of spectral index in a given band during a flare depends on the relationship of the acceleration and cooling timescales for electrons which emit in that band. Where the acceleration timescale is much shorter than the cooling timescale, higher-energy emissions should lead lower-energy emissions (Georganopoulos & Marscher 1998, Takahashi et al. 1999), so that a flare will propagate from the highest energies to lower energies. But if the cooling and acceleration timescales are close to equal near where the peak in νF_ν is, the relationship between spectral changes is complex. In that case, at low energies, where the acceleration timescale is much faster than the cooling timescale (note that $t_{cool} \propto E_\gamma^{-1/2}$ for synchrotron radiation), their model predicts a spectral flattening in advance of the flux maximum, peaking slightly before flux maximum, followed by a decrease to values somewhat below the jet's nominal value after maximum flux, and then a return to the nominal value after the disturbance has passed. But at high energies, where $t_{cool} \sim t_{acc}$, a spectral *steepening* is predicted in advance of the flux maximum, followed by a hardening as the number of newly accelerated electrons build up. Under this model (assuming no injection of fresh particles), flares represent the reacceleration of old particles within the jet, so they will propagate from low to high energies, *i.e.* observed spectral changes at higher energies

will lag those at lower energies. We appear to be observing *both* situations at different locations in the optical emission from the M87 jet, perhaps not dissimilar from what has been seen (on shorter timescales) in blazars; in particular recent observations of PKS 2155–304 several examples of both types of flares were seen within a week of observation (Sambruna et al. 1999).

6.4. Comparison to Radio-Optical Spectral Analysis for Other Jets

With the above data and analysis in mind we can compare our findings to those of other teams on various optical jets. Unfortunately high-quality data (either ground-based or HST) are few and far between, and only exist on a few sources.

The only other radio/optical jet to have been imaged polarimetrically with HST is 3C 273. Comparing the HST and radio polarimetry for its jet (Thomson, Mackay & Wright 1993, Conway et al. 1993), 3C 273 seems to show more similarity between radio and optical polarized structure than does the M87 jet (P99), despite having a large number of knots. However, a deep comparison of its radio and optical polarized structure is currently impossible because of the low signal to noise of the existing, pre-COSTAR FOC polarimetry data. Further, a deep analysis of its optical spectrum has not yet been done, so we need to rely on ground-based data to compare the polarized and spectral index maps. Neumann, Meisenheimer & Röser (1997) and Röser & Meisenheimer (1991) have carried out a deep analysis of the near-IR to optical spectrum of the 3C273 jet (note that the latter paper also contains ground-based polarimetry, which is also useful), which fortunately is largely unaffected by galaxy subtraction issues (unlike ground-based work for M87). They find considerably more variation in α_o than α_{ro} for 3C 273, as we do for M87, and also find that 3C 273's jet is significantly narrower in the optical than in the radio (as we do for M87; see SBM96). A more recent, preliminary comparison of the deep HST/WFPC2 and radio images (Röser et al. 1997, Jester et al. in prep.) show some other differences between the jet's optical and radio structure: the optical jet appears to stop 1" short of the terminal radio hotspot, and the optical and radio flux maxima of knot B are not spatially coincident. Interestingly, they

also find somewhat of an anti-correlation between optical polarization and spectral index structure, with low polarization and fairly flat spectral indices $12 - 14''$ from 3C 273's nucleus, but higher polarization and much steeper spectral indices further out. More recently, *Chandra* has imaged the 3C273 jet, finding a rather different morphology in X-rays than either the optical or radio: one knot's flux maximum appears displaced, and the optical emission declines drastically in the knot D-H region, where the strongest radio emission is seen, analysis of the knots' spectra reveal inconsistencies between the spectra of downstream knots and the predictions of SSC models (Marshall et al. 2000). Further analysis and deeper comparisons of the X-ray, optical and radio structure of the 3C 273 jet will no doubt give us considerable insight into its physics.

Lara et al. (1999) find a steep optical spectrum for 3C264's jet, and a broadband shape consistent with either the CI model or a significantly sub-equipartition magnetic field (Heinz & Begelman 1997), and that it is unlikely that the observed optical jet emissions are inverse-Compton in origin. They invoke the lack of well-defined knots in the 3C264 jet as evidence against Fermi acceleration in shocks. This, plus the much earlier deceleration found for the 3C264 jet (Lara et al. 1999, Baum et al. 1997), are key distinctions between it and M87, which may make 3C264 more amenable to the CI scenario than M87, where several bright shocks are observed. High signal to noise X-ray or UV observations, as well as deeper HST imaging data in several bands (the HST data analyzed by Lara et al. were 300s snapshots), as well as HST polarimetry, would go a long way towards resolving the mechanism which dominates in the 3C264 jet.

Schwartz et al. (2000) and Chartas et al. (2000) have discussed the discovery with *Chandra* of an X-ray jet in the quasar PKS 0637 – 752, and the subsequent identification of optical emission from three knots in its jet in deep HST images of the field. This object is at much larger distances than 3C 273, let alone M87 or 3C 264, making detailed comparisons of structure difficult. However, comparisons of the structure in the radio and optical reveal large-scale correspondence but tantalizing hints of differences on scales of $\sim 0.2''$ which require deeper investigation. The broadband spec-

tra of the knots are also inconsistent with the predictions of simple SSC models, although Comptonized emission from CMB photons remains a possibility (Tavecchio et al. 2000)

One final object for which such analysis can in future be done is 3C 66B. Sparks et al. (in prep.) are analyzing radio-optical spectral data for this object, which also shows interesting radio-optical spectral differences.

By discussing the kinetic energy budget of optical jets, Scarpa & Urry (1999) find that their observed properties require either fairly high bulk Doppler factors $\Gamma \sim 5$ and viewing angles $\lesssim 25^\circ$ (if equipartition is maintained), or magnetic fields significantly less strong than equipartition (whereupon lower values of Γ or larger viewing angles are possible). This is in agreement with the findings of Heinz & Begelman (1997) for M87, and consistent with our results. A similar result has been found through comparison of the properties of dust disks in the 3CR sample (Sparks et al. 2000).

7. Scope for Future Observations

The above sections underline the importance of future observations. Since our data indicate break frequencies significantly in excess of 10^{15} Hz, high-resolution imaging observations in the far UV and X-rays are now required to localize the peak of the synchrotron emission from bright knots in the jet. Such data, if gathered contemporaneously with optical and radio observations, would allow much stronger constraints on synchrotron emission and particle acceleration models.

The *Chandra* observations are particularly critical in this regard. Those observations will yield spatially resolved (resolution $\sim 0.7''$) spectra in the $0.1 - 10$ keV region (*i.e.*, $2 - 200 \times 10^{16}$ Hz), allowing direct comparisons of optical and radio morphologies. Such comparisons will directly test the findings of Neumann et al. (1997) that the X-ray emission from knot A is not coincident with the radio/optical peak, and will allow us to localize sites of particle acceleration. The *Chandra* observations will also directly test the nature of the jet's X-ray emission by measuring the X-ray slope (§5.1).

Our data indicate that observations in the far-UV are required to localize the synchrotron peak of much of the jet. No imaging mission is cur-

rently proposed at these wavelengths; however, the prospects for detecting M87 in the far-UV are bright, since the $N(H)$ along its line of sight is relatively low (although EUVE did not detect M87; Lampton et al. 1997).

Future monitoring experiments will have unparalleled importance for models of jet flares in blazars (for a review of the spectral evolution observed in HBL flares, see Takahashi et al. 1999). Once the timescale of X-ray variability is established, the combination of contemporaneous VLA, HST and *Chandra* observations will make it possible to for the first time map out the broadband spectrum and polarization of a flaring component, and watch its spectrum decay once the flare has passed. Such a study would allow us to fully model the spectrum and magnetic field configuration in the flaring region.

We wish to thank Eddie Bergeron and Megan Sosey, as well as Shireen Gonzaga, for considerable help with the HST data reductions. We also wish to thank our referee, Hermann-Josef Röser, for many suggestions which significantly improved this paper. JPL thanks the STScI for hospitality during his sabbatical visit. ESP thanks Chris Reynolds, Sebastian Heinz, Mitch Begelman, Joel Carvalho, Tim Heckman, Julian Krolik, Eric Agol, Greg Madejski and Jean Eilek for interesting discussions. Research on M87 at STScI is supported by HST grants GO-5941, GO-7274, GO-7866, GO-8048 and GO-8140. ESP acknowledges support at Johns Hopkins University and the University of Maryland, fromfromfrom NASA LTSA grant NAG5-9534/NAG5-9997.

REFERENCES

Allen, S. W., DiMatteo, T., & Fabian, A. C., 2000, MNRAS 311, 492.

Baggett, S., Casertano, S., Gonzaga, S., & Ritchie, C., 1997, WFPC-2 ISR 97-10.

Baggett, S., & Gonzaga, S., 1998, WFPC-2 ISR 98-03.

Biretta, J. A., Owen, F. N., & Hardee, P. E., 1983, ApJL 274, L27.

Biretta, J. A., Sparks, W. B., & Macchetto, F. D., 1999, ApJ, 520, 621 (BSM99).

Biretta, J. A., Perlman, E. S., Sparks, W. B., & Macchetto, F. D., 1999, in *The Radio Galaxy M87*, Springer-Verlag Lecture Notes in Physics, ed. H.-J. Roeser & K. Meisenheimer, p. 100

Biretta, J. A., Stern, C. P., & Harris, D. E., 1991, AJ 101, 1632 (BSH91).

Boksenberg, A., et al. 1992, A&A 261, 393.

Boroson, T. A., & Thompson, I. B., 1991, AJ 101, 111.

Calzetti, D. & Gilmore, D., 1998, NICMOS ISR 98-002.

Capetti, A., Macchetto, F. D., Sparks, W. B., & Biretta, J. A., 1997, A&A 317, 637.

Carilli, C. L., Perley, R. A., Dreher, J. W., & Leahy, J. P., 1991, ApJ 383, 554

Casertano, S., et al., 1999, in prep.

Chartas, G., et al. 2000, ApJ in press, astro-ph/0005227.

Colina, L., Holfeltz, S., & Ritchie, C., 1998, in *NICMOS and the VLT: a new era of High-Resolution Imaging and Spectroscopy*, ed. W. Freudling & R. Hook (ESO, Garching).

Conway, R. G., Garrington, S. T., Perley, R. A., & Biretta, J. A., 1993, A & A 267, 347.

Cox, C., Ritchie, C., Bergeron, L. E., Mackenty, J., & Noll, K., 1997, STScI Calibration Report OSG-CAL-97-07.

Fruchter, A. S., & Hook, R. N., 1998, PASP, in press (astro-ph/9808087).

Georganopoulos, M., & Marscher, A. P., 1998, ApJ 506, L11.

Gonzaga, S., et al., 1998, “The Drizzling Cookbook”, WFPC2 ISR 98-04.

Guainazzi, M., & Molendi, S., 1999, A & A, in press (astro-ph/9910271).

Harris, D. E., Biretta, J. A., & Junor, W., 1997, MNRAS 284, L21.

Harris, D. E., Biretta, J. A., & Junor, W., 1998, in *The Radio Galaxy M87*, Springer-Verlag Lecture Notes in Physics, ed. H.-J. Roeser & K. Meisenheimer, p. 319.

Heavens, A., & Meisenheimer, K., 1987, MNRAS 225, 335

Heinz, S., & Begelman, M. C., 1997, ApJ 490, 633.

Holtzman, J. A., et al., 1995, PASP 107, 156.

Jaffe, W. J., & Perola, G. C., 1973, A&A 26, 421.

Kardashev, N. S., 1962, Soviet Astronomy – AJ 6, 317.

Keel, W. C., 1988, ApJ 329, 532

Killeen, N. E., Bicknell, G. V., Hyland, A. R., & Jones, T. J., ApJ 280, 126.

Kirk, J. G., Rieger, F. M., & Mastichiadis, A., 1998, A & A 333, 452.

Kubo, H., Takahashi, T., Madejski, G., Tashiro, M., Makino, F., Inoue, S., & Takahara, F., 1998, ApJ 504, 693.

Lampton, M., Lieu, R., Schmitt, J. H. M., Bowyer, S., Voges, W., Lewis, J., & Wu, X., 1997, ApJS 108, 545.

Leahy, J. P., 1991, in “Beams and Jets in Astrophysics”, ed. P. A. Hughes (Cambridge: Cambridge University Press), p. 100.

Lesch, H., & Birk, G. T., 1998, ApJ 499, 167.

Mackenty, J., Skinner, C., & Bushouse, H., 1997, NICMOS ISR-029.

Marshall, H. L., et al., 2000, preprint.

Matsumoto, H., et al. 1996, PASJ 48, 201.

Meisenheimer, K., Roeser, H.-J., & Shlötelburg, M., 1996, A&A 307, 61 (MRS96).

Meisenheimer, K., Roeser, H.-J., Hiltner, P., Yates, M. G., Longair, M. S., Chini, R., & Perley, R. A., 1989, A&A 219, 63.

Meisenheimer, K., Yates, M. G., & Röser, H.-J., 1997, A&A 325, 57.

Neumann, M., Meisenheimer, K., & Röser, H.-J., 1997, A & A 326, 69.

Neumann, M., Meisenheimer, K., Röser, H.-J., & Fink, H. H., 1997, A & A 318, 383.

NICMOS team, “NICMOS Photometry Update,” 1999,
http://www.stsci.edu/instruments/nicmos/nicmos_doc.phot.html

Owen, F. N., Hardee, P. E., & Cornwell, T. J., 1989, 340, 698.

Pacholczyk, A. G., 1970, Radio Astrophysics (San Francisco: Freeman).

Perez-Fournon, L., Colina, L., Gonzales-Serrano, J. I., & Biermann, P. L., 1988, ApJ 329, L81.

Perlman, E. S., Biretta, J. A., Zhou, F., Sparks, W. B., & Macchetto, F. D., 1999, AJ 117, 2185 (P99).

Perlman, E. S., Stocke, J. T., Wang, Q. D., & Morris, S. L., 1996, ApJ 456, 451.

Perola, G. C., & Tarenghi, M., 1980, ApJ 240, 447.

Reynolds, C. S., Heinz, S., Fabian, A. C., & Begelman, M. C., 1999, ApJ 521, 99.

Röser, H.-J., & Meisenheimer, K., 1991, A & A 252, 458.

Röser, H.-J., Meisenheimer, K., Neumann, M., Conway, R. G., Davis, R. J., & Perley, R. A., 1997, Rev. Mod. Ast. 10, 253.

Sambruna, R. M., Maraschi, L., & Urry, C. M., 1996, ApJ 463, 444.

Sambruna, R. M., 1999, astro-ph/9912060.

Schreier, E. J., Gorenstein, P., & Feigelson, E. D., 1980, ApJ 261, 42.

Schwartz, D. A., et al., ApJL 2000 in press, astro-ph/0005255.

Smith, R. M., Bicknell, G. V., Hyland, A. R., & Jones, T. J., 1983, ApJ 266, 68.

Sosey, M., & Bergeron, E., 1999, NICMOS ISR 99-008.

Sparks, W. B., Baum, S. A., Biretta, J., Macchetto, F. D., & Martel, A. R., 2000, ApJ in press, astro-ph/0007358.

Sparks, W. B., Biretta, J. A., & Macchetto, F., 1996, ApJ 473, 254 (SBM96).

Sparks, W. B., Ford, H. C., & Kinney, A. L., 1993, ApJ 413, 531.

Stocke, J. T., Rieke, G. H., & Lebofsky, M. J., 1981, Nature 294, 319.

Storrs, A. D., Bergeron, L. E., & Holfeltz, S. T., 1999, NICMOS ISR 99-002.

Takahashi, T., Madejski, G., & Kubo, H., 1999, Astroparticle Physics 11, 177.

Tavecchio, F., Maraschi, L., Sambruna, R. M., & Urry, C. M., 2000, ApJ in press, astro-ph/0007441.

Thomson, R. C., Mackay, C. D., & Wright, A. E., 1993, Nature 365, 133.

Tonry, J. L., 1991, ApJ 373, L1.

van der Marel, R., 1998, <http://sol.stsci.edu/software/pedestal.html>.

Whitmore, B. & Heyer, I., 1995, WFPC-2 ISR 95-04.

Whitmore, B. & Heyer, I., 1997, WFPC-2 ISR 97-08.

Zhou, F., 1998, PhD Thesis, New Mexico Institute of Mining & Technology.

Figure Captions

Figure 1. The jet of M87, as seen by HST, in the F300W (0.3 microns, top), F814W (0.8 microns, middle) and F160W (1.6 microns, bottom) bands. Flux levels displayed are from -0.3 to 1 $\mu\text{Jy}/\text{pix}$ for the F300W image, -0.5 to 2 $\mu\text{Jy}/\text{pix}$ for the F814W image, and -1 to 4 $\mu\text{Jy}/\text{pix}$ for the F160W image, and within these limits the identical color scale (shown at bottom) was used for all three images. The images have been rotated so that the jet is along the X axis, and have identical pixel sizes, origins and orientations. The traditional names are used for bright knots.

Figure 2. Maps of fitted quantities for the M87 jet, with the convolved F814W image of the jet shown for comparison at the bottom. At top (Figure 2a), we show the optical spectral index image; second from top (Figure 2b), we show the radio-optical spectral index image. We also show maps of the synchrotron break frequency (third from top, Figure 2c) and injection index (fourth from top, Figure 2d) in the KP model. Identical color tables were used for all panels. The color scale in Figure 2a runs from 1.2 to 0.4, while that in Figures 2b and 2d run from 0.85 to 0.6, and that for the break frequency map (Figure 2c) runs from 10^{15} to 10^{16} .

Figure 3. Runs of α_o (top, Fig. 3a), α_{ro} (second from top, Fig. 3b), $\alpha_o - \alpha_{ro}$ (third from top, Fig. 3c) and F814W flux (bottom, Fig. 3d), plotted as a function of distance along the jet axis. In this Figure we show the inner regions of the jet, out to $10''$ from the nucleus. These values are *flux-weighted*, i.e., flux is summed across the jet at each pixel in the x direction before spectral indices were computed. See §§3 for discussion.

Figure 4. Runs of α_o (top, Fig. 4a), α_{ro} (second from top, Fig. 4b), $\alpha_o - \alpha_{ro}$ (third from top, Fig. 4c) and F814W flux (bottom, Fig. 4d), plotted as a function of distance along the jet axis. In this Figure we show the outer regions of the jet, $10 - 20''$ from the nucleus. These values are *flux-weighted*, i.e., flux is summed across the jet at each pixel in the x direction before spectral indices were computed. See §§3 for discussion.

Figure 5. Fluxes of knot regions. The regions are defined in Table 2. The error bars include flatfielding, zeropoint and Poisson errors. Best-fit power law spectra are shown as lines on these

log-log plots, and the spectral indices are given in Table 2.

Figure 6. Synchrotron spectrum model fits to four regions of the jet: knot D (Figure 6a), knot A (Figure 6b), knot B (Figure 6c), and knots A+B+C (Figures. 6d-e). Along with our data, we plot fits from the JP, KP and CI models, both including and not including the X-ray point. In Figures 6d-e, we show also previous data as tabulated by MRS96 (see references and discussion in that paper). In all plots, data from this work are plotted as diamonds; in Figs. 6d-e, data taken from MRS96 are plotted as squares. See §4 for discussion.

This figure "spec98_3_fig1.gif" is available in "gif" format from:

<http://arxiv.org/ps/astro-ph/0012044v1>

This figure "spec98_3_fig2.gif" is available in "gif" format from:

<http://arxiv.org/ps/astro-ph/0012044v1>

TABLE 1
LOG OF HST OBSERVATIONS

Band	λ_{eff}	$\Delta\lambda$	Date	Integration Time	Pixel scale	Dither amount
F300W	2993	727.6	25 Feb 1998	800 ¹	0.0455	N/A
F450W	4557	925.0	25 Feb 1998	520 ¹	0.0455	N/A
F606W	6001	1578.7	25 Feb 1998	520 ¹	0.0455	N/A
F814W	7996	1758.0	25 Feb 1998	1400 ²	0.03217 ³	0.3539 ²
F110W	11292	3000	26 Feb 1998	1792 ⁴ / 768 ⁵	0.0432025	1.4
F160W	16071	2000	26 Feb 1998	1792 ⁴ / 768 ⁵	0.0432025	1.4
F205W	20714	3000	4 Apr 1998	4352 ⁶	0.0758667	2

¹Observation was CR-split

²Dithered to 3 positions; CR-split at middle position only

³Observation was drizzled onto a grid with this pixel size

⁴Observation time on inner jet, split among 2 positions separated by 1.4 arcsec

⁵Observation time on outer jet, split among 2 positions separated by 1.4 arcsec

⁶Two observations taken, dithered by 2 arcsec

TABLE 2
PHOTOMETRIC DATA

Knot	X ¹	Y ¹	F(Radio) ²	F(F205W) ¹	F(F160W)	F(F110W)	F(F814W)	F(F606W)	F(F450W)	F(F300W)	α_o	α_{ro}
HST-1	28-45	198-203	35640 \pm 690	... ³	41.9 \pm 2.0	32.8 \pm 1.9	24.0 \pm 0.9	19.8 ⁴ \pm 0.6	18.3 ⁴ \pm 0.6	9.0 ⁴ \pm 0.4	-1.02 \pm 0.09	-0.71
D	52-79	192-205	161540 \pm 1920	280 \pm 11	224 \pm 9	168 \pm 7	150 \pm 4	117 \pm 3	96.2 \pm 2.5	59.5 \pm 1.6	-0.86 \pm 0.06	-0.69
D-East	52-63	195-205	90630 \pm 1120	143 \pm 6	119 \pm 5	97.6 \pm 4.2	85.3 \pm 2.2	66.2 \pm 1.7	56.6 \pm 1.5	36.5 \pm 1.0	-0.78 \pm 0.05	-0.70
D-Middle	63-70	193-200	48270 \pm 660	70.4 \pm 3.0	58.5 \pm 2.5	46.5 \pm 2.1	35.7 \pm 1.0	28.6 \pm 0.8	22.2 \pm 0.6	13.3 \pm 0.4	-0.96 \pm 0.06	-0.71
D-West	63-70	195-203	30470 \pm 620	56.7 \pm 2.6	46.6 \pm 2.1	33.0 \pm 1.8	29.7 \pm 0.9	23.0 \pm 0.7	18.8 \pm 0.6	11.0 \pm 0.4	-0.93 \pm 0.07	-0.68
E	97-109	193-202	48050 \pm 810	71.8 \pm 3.2	67.2 \pm 2.0	42.9 \pm 2.3	42.3 \pm 1.3	33.4 \pm 0.9	28.0 \pm 0.8	16.2 \pm 0.6	-0.88 \pm 0.08	-0.71
F	123-147	191-207	144900 \pm 1860	262 \pm 11	271 \pm 11	147 \pm 6	158 \pm 5	123 \pm 3	98.8 \pm 2.6	62.7 \pm 1.7	-0.84 \pm 0.08	-0.69
I	162-173	191-205	75800 \pm 1070	131 \pm 5	138 \pm 6	88.2 \pm 3.9	70.7 \pm 2.0	54.2 \pm 1.5	45.6 \pm 1.2	28.6 \pm 0.8	-0.88 \pm 0.05	-0.69
A	173-201	180-220	1218000 \pm 12000	2633 \pm 105	2344 \pm 90	1829 \pm 73	1363 \pm 34	1086 \pm 27	904 \pm 23	586 \pm 15	-0.84 \pm 0.03	-0.67
A bar	173-178	180-220	103990 \pm 1370	241 \pm 10	222.3 \pm 9.1	148.5 \pm 6.3	107.7 \pm 2.9	83.8 \pm 2.2	65.5 \pm 1.7	40.3 \pm 1.1	-0.99 \pm 0.03	-0.66
A shock	179-188	180-220	702700 \pm 7100	1495 \pm 60	1325 \pm 53	1105 \pm 44	826 \pm 21	670 \pm 17	564 \pm 14	373.2 \pm 9.4	-0.78 \pm 0.04	-0.67
A diffuse	189-201	180-220	411400 \pm 4300	896 \pm 36	797 \pm 32	576 \pm 23	429 \pm 11	332.6 \pm 8.4	274.3 \pm 6.9	172.6 \pm 4.4	-0.91 \pm 0.03	-0.67
B	202-233	180-220	808400 \pm 8300	1739 \pm 70	1489 \pm 60	1104 \pm 44	811 \pm 20	623 \pm 16	504 \pm 13	306.8 \pm 7.8	-0.96 \pm 0.03	-0.67
B-1	202-218	191-205	535000 \pm 5400	1021 \pm 41	901 \pm 36	692 \pm 28	519 \pm 13	400 \pm 10	321.2 \pm 8.0	193.1 \pm 4.9	-0.96 \pm 0.95	-0.68
B-2	218-233	185-204	248600 \pm 2700	563 \pm 23	456 \pm 18	348 \pm 14	248.0 \pm 6.3	189.4 \pm 4.8	153.4 \pm 3.9	91.9 \pm 2.4	-0.99 \pm 0.03	-0.66
C-1	242-260	191-220	544700 \pm 5600	971 \pm 39	797 \pm 32	606 \pm 24	415 \pm 10	310.7 \pm 7.8	241.0 \pm 6.1	135.9 \pm 3.5	-1.10 \pm 0.05	-0.69
C-2	261-270	188-225	164000 \pm 2000	313 \pm 13	238.9 \pm 9.8	185.4 \pm 7.8	115.7 \pm 3.1	86.3 \pm 2.3	68.1 \pm 1.8	37.6 \pm 1.1	-1.14 \pm 0.04	-0.68
A+B+C	173-274	173-227	2895000 \pm 29000	5850 \pm 230	4980 \pm 200	3740 \pm 150	2736 \pm 69	2137 \pm 54	1761 \pm 44	1085 \pm 27	-0.92 \pm 0.03	-0.67

¹Box coordinates are in pixels, with the jet along the x axis, a scale of 0.0758667"/pix, and the nucleus at (20,200).

²All fluxes are in μ Jy.

³Region is partly off the F205W image because of a poor orientation. See §2.

⁴Knot HST-1 is likely obscured by a dust lane and hence the fluxes in the short wavelength bands may be low. See §2.

TABLE 3
BEST-FIT PARAMETERS FOR SYNCHROTRON SPECTRUM MODELS

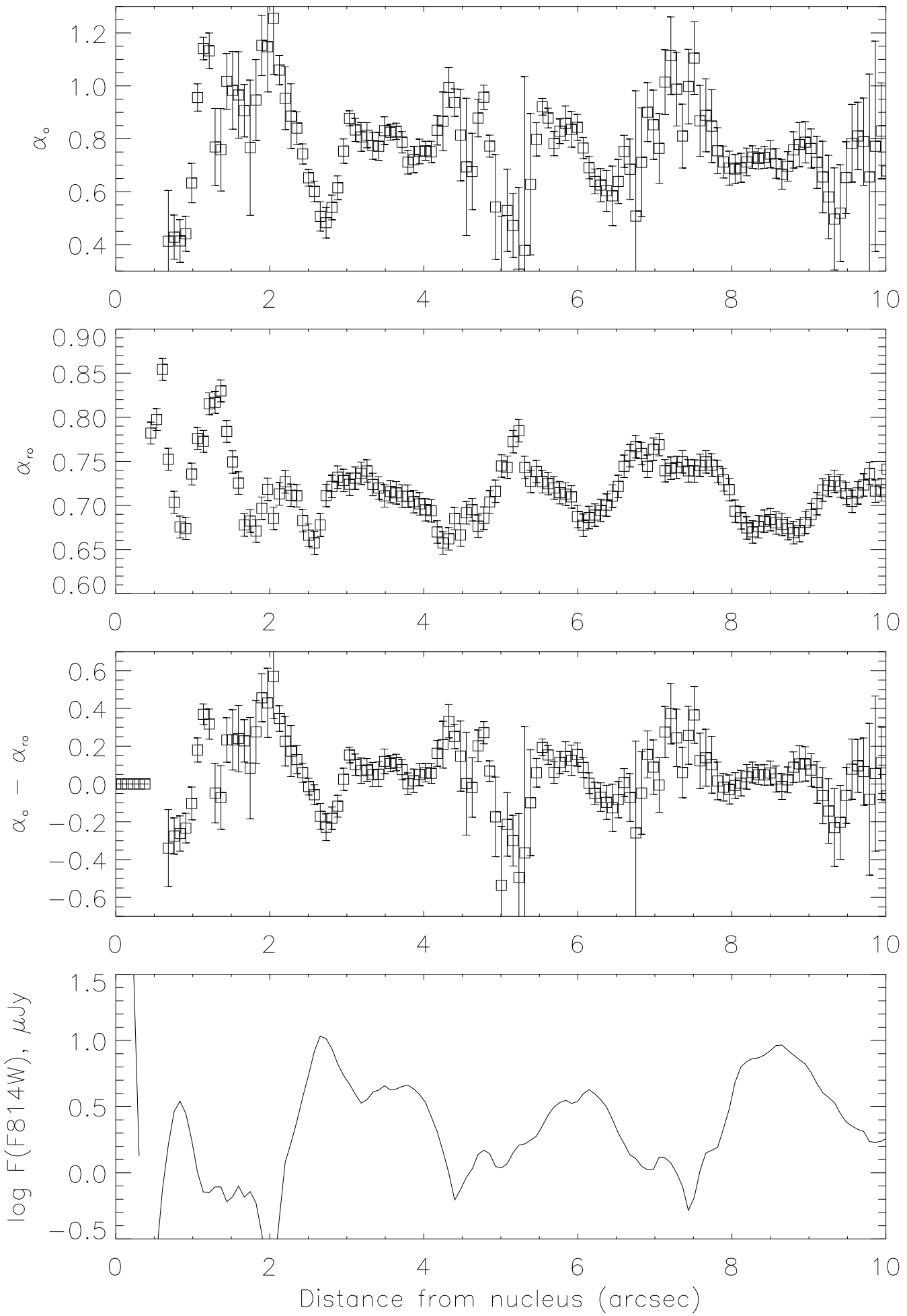
Knot	α_{inj}	JP Model	KP Model	CI Model
D ¹	0.690 ³	$\nu_B = 6.85 \pm 0.29 \times 10^{16}$ Hz $\chi^2 = 4.34$	$1.72 \pm 0.21 \times 10^{16}$ Hz 5.67	$4.32 \pm 0.64 \times 10^{15}$ Hz 30.88
	0.692 ⁴	$\nu_B = 6.94 \pm 0.29 \times 10^{16}$ Hz $\chi^2 = 4.83$	$1.85 \pm 0.31 \times 10^{16}$ Hz 6.89	$4.74 \pm 0.73 \times 10^{15}$ Hz 32.49
A ¹	0.666 ³	$\nu_B = 8.31 \pm 0.25 \times 10^{16}$ Hz $\chi^2 = 4.00$	$2.38 \pm 0.18 \times 10^{16}$ Hz 3.37	$3.17 \pm 0.34 \times 10^{15}$ Hz 32.37
	0.645 ⁴	$\nu_B = 7.45 \pm 0.20 \times 10^{16}$ Hz $\chi^2 = 28.08$	$1.30 \pm 0.10 \times 10^{16}$ Hz 16.771	$1.26 \pm 0.09 \times 10^{15}$ Hz 21.37
B ¹	0.667 ³	$\nu_B = 3.99 \pm 0.13 \times 10^{16}$ Hz $\chi^2 = 18.31$	$4.09 \pm 0.30 \times 10^{15}$ Hz 8.04	$1.63 \pm 0.13 \times 10^{15}$ Hz 55.54
	0.646 ⁴	$\nu_B = 3.66 \pm 0.11 \times 10^{16}$ Hz $\chi^2 = 62.83$	$2.02 \pm 0.09 \times 10^{15}$ Hz 1.24	$7.61 \pm 0.42 \times 10^{14}$ Hz 49.24
A+B+C ²	0.673 ³	$\nu_B = 7.05 \pm 0.36 \times 10^{16}$ Hz $\chi^2 = 15.54$	$1.02 \pm 0.11 \times 10^{16}$ Hz 6.96	$2.47 \pm 0.24 \times 10^{15}$ Hz 12.41
	0.644 ⁴	$\nu_B = 5.76 \pm 0.24 \times 10^{16}$ Hz $\chi^2 = 97.04$	$2.09 \pm 0.10 \times 10^{15}$ Hz 17.04	$6.87 \pm 0.34 \times 10^{14}$ Hz 7.57

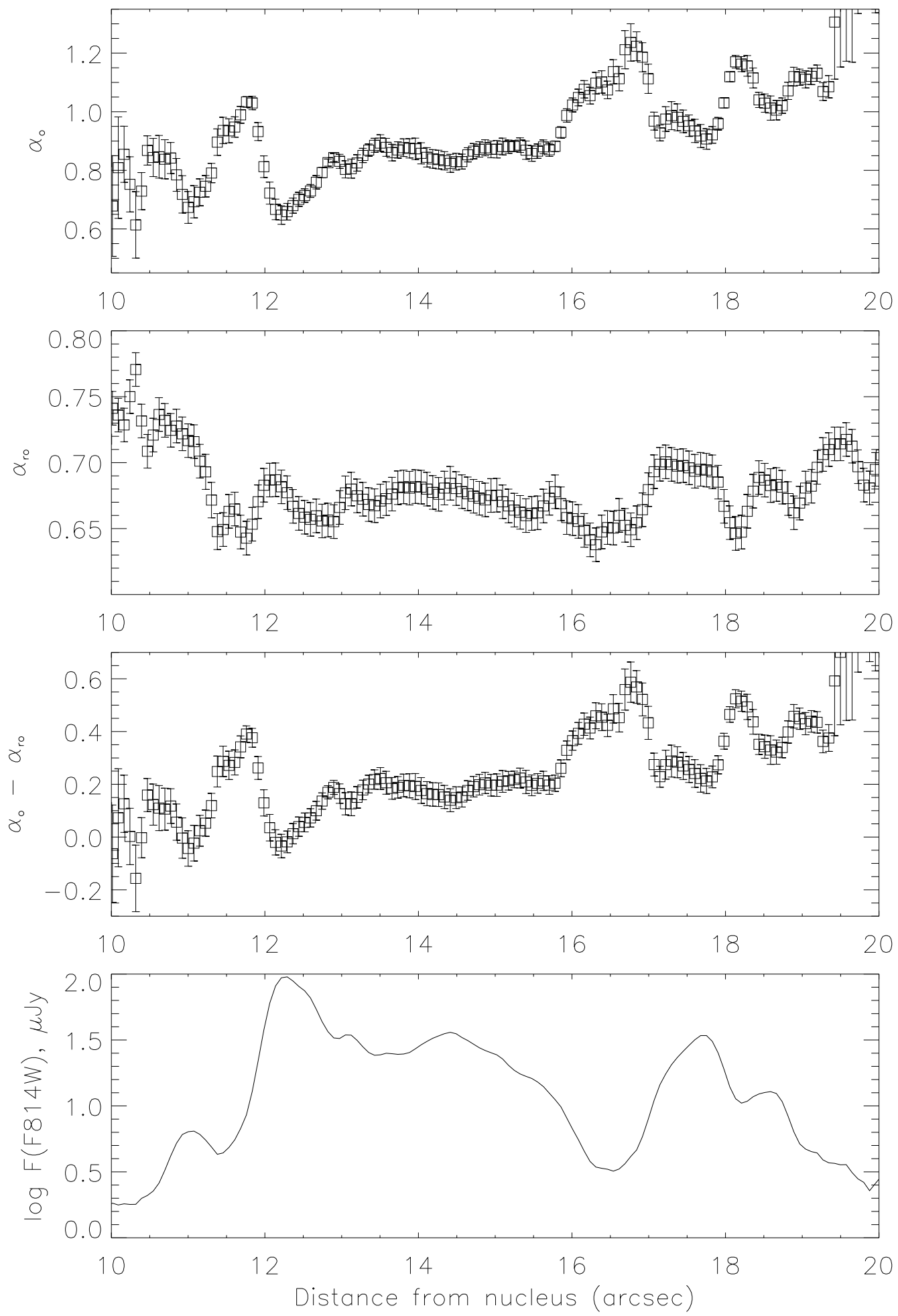
¹1998 data, 9 frequencies.

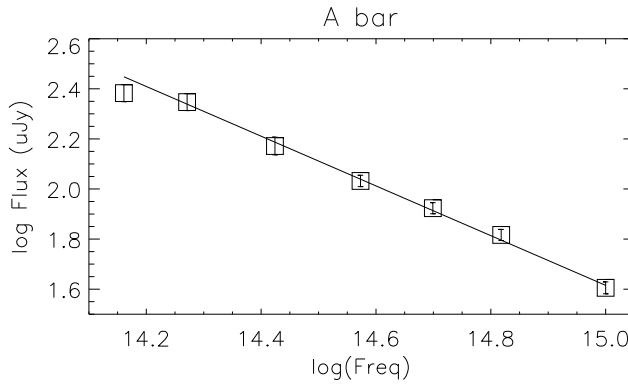
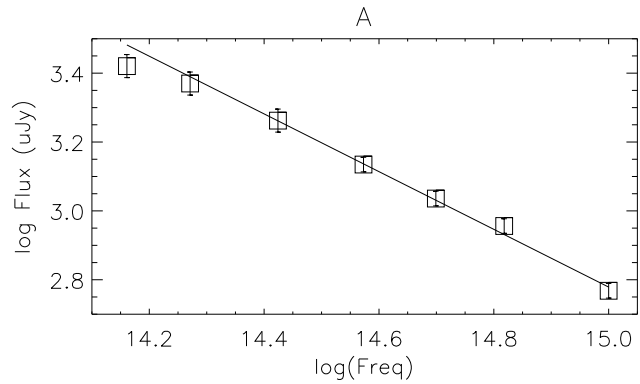
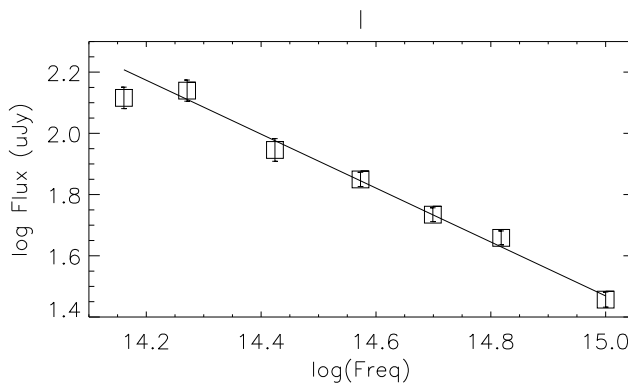
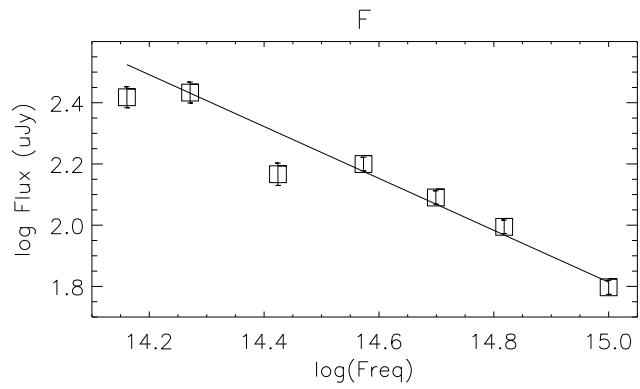
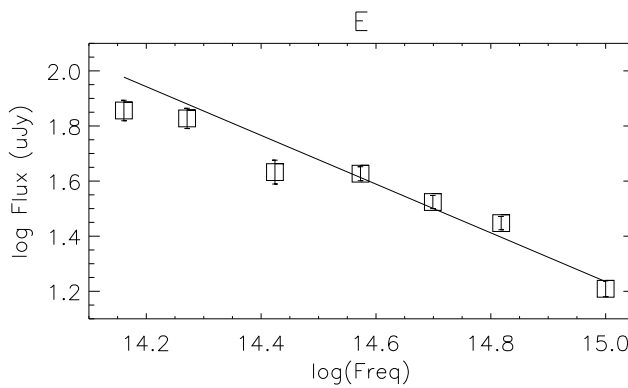
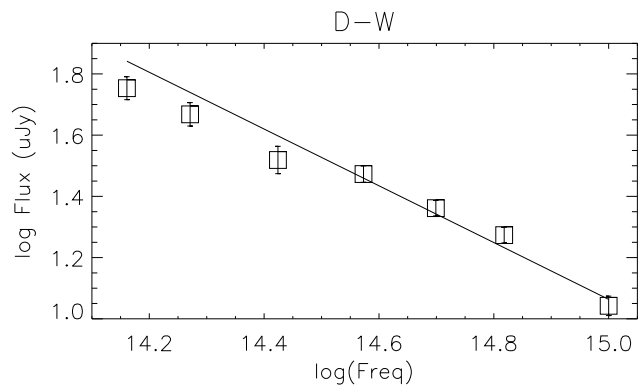
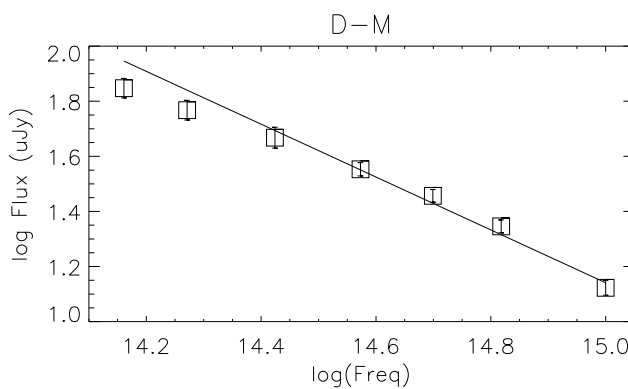
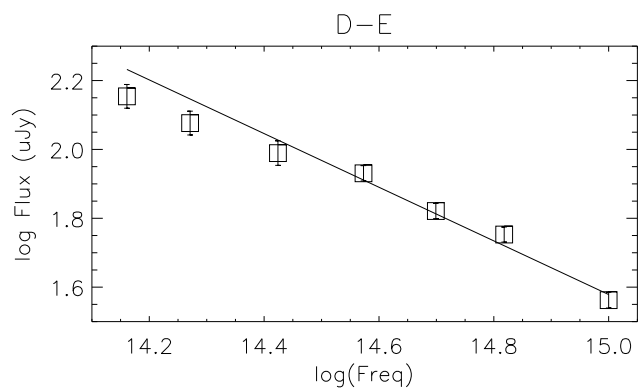
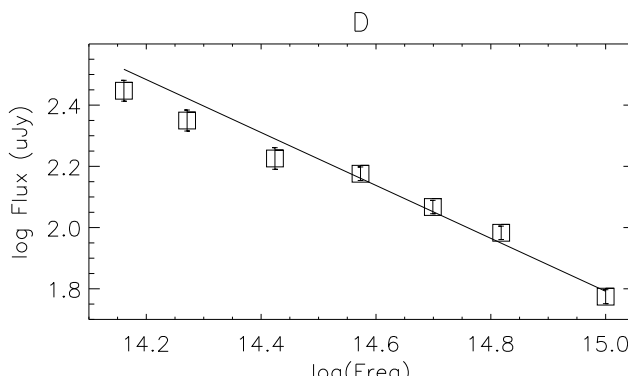
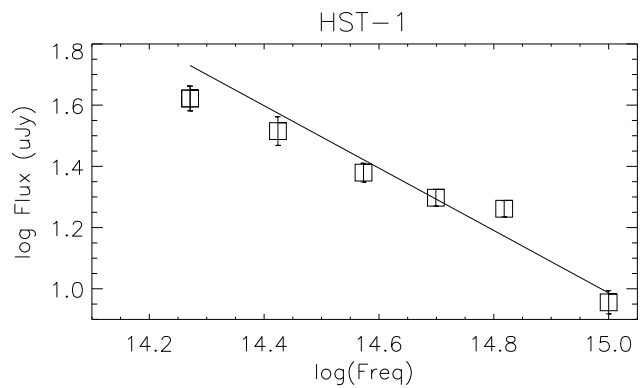
²Data from Meisenheimer et al. (1996), 24 frequencies.

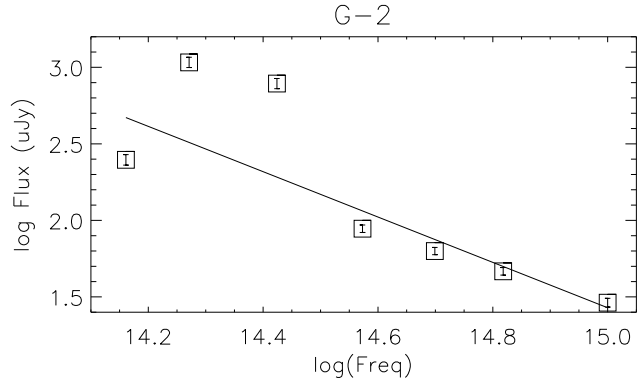
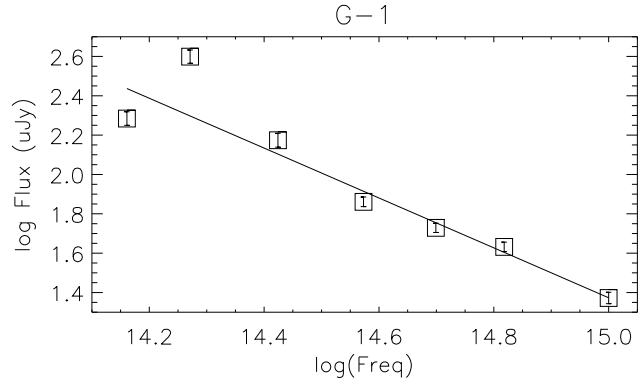
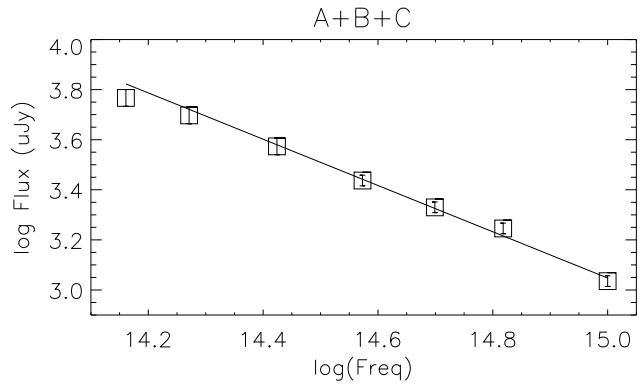
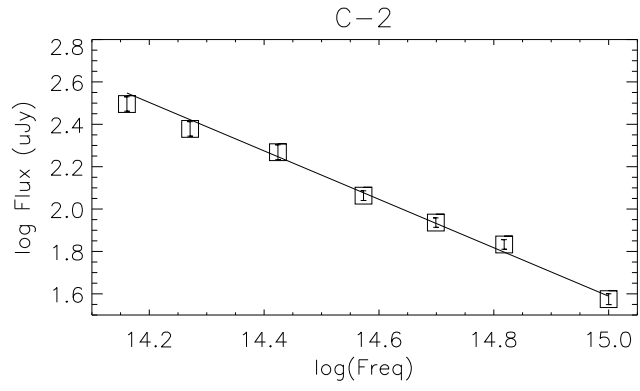
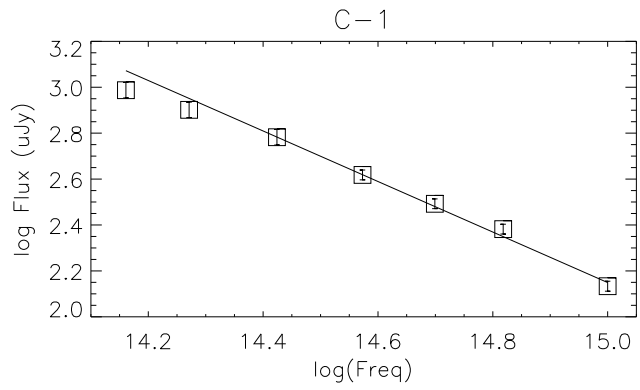
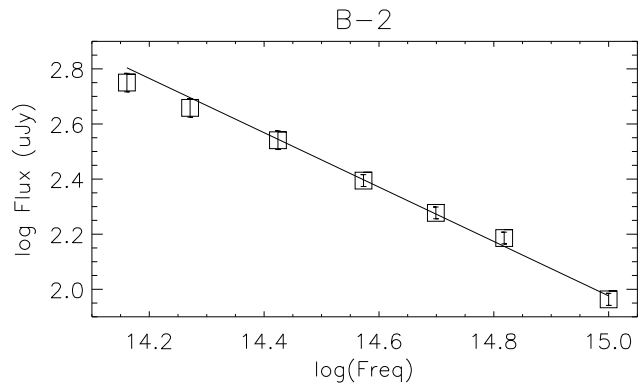
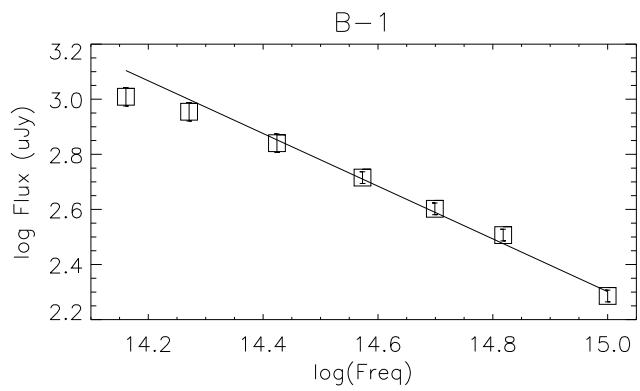
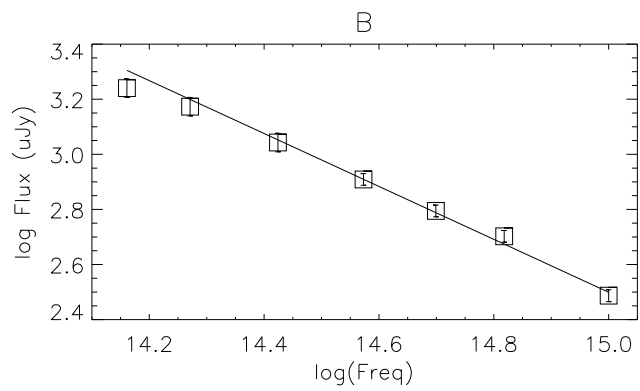
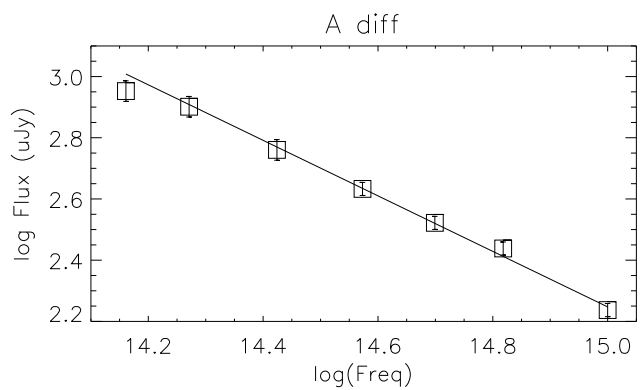
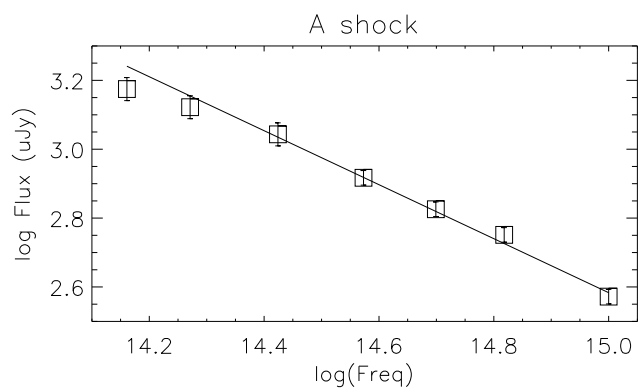
³Average value of α_{ro} for this region taken from Table 2.

⁴Average value of α_{in} for this region from the map of α_{in} , Fig. 2d.

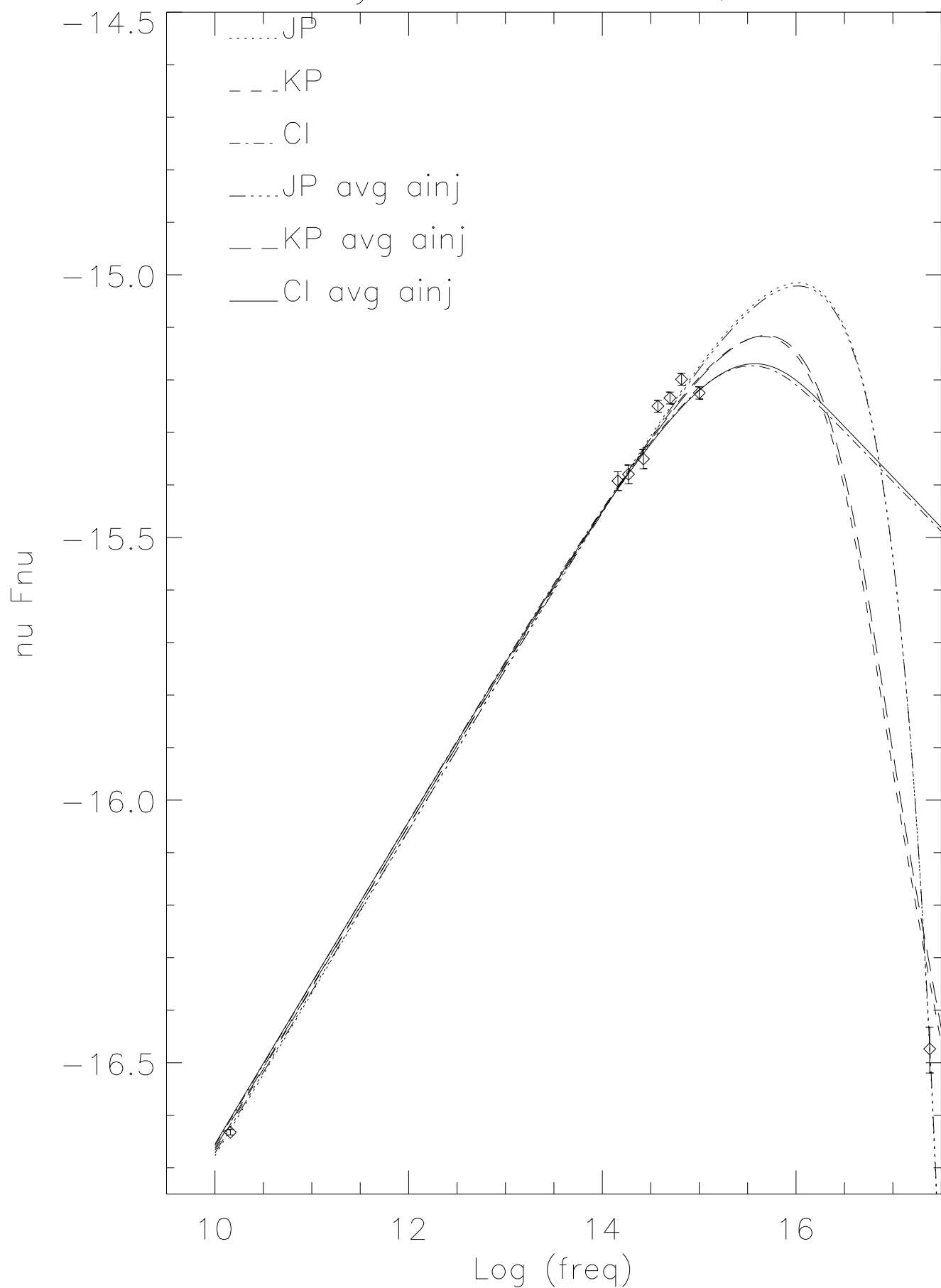




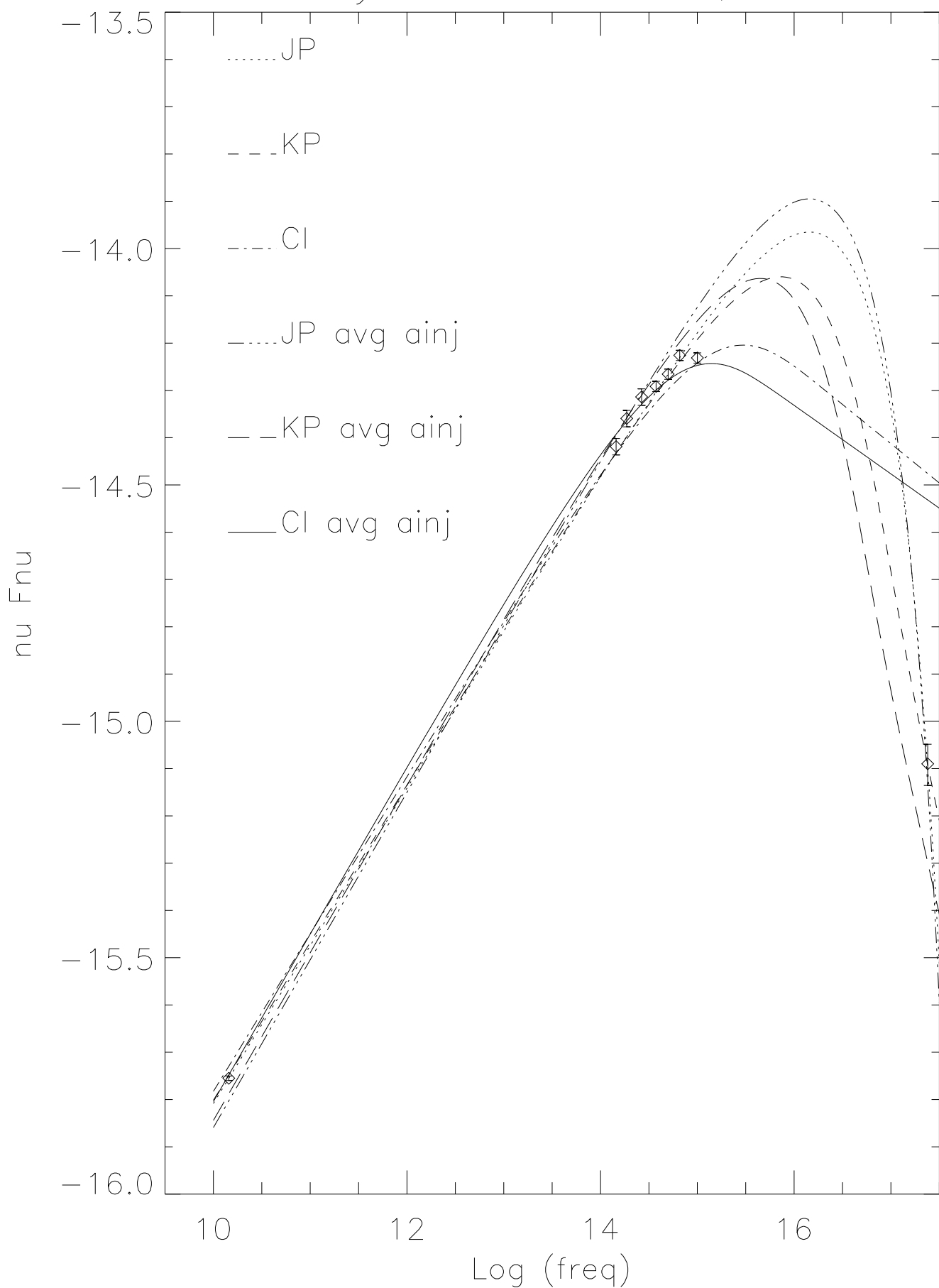




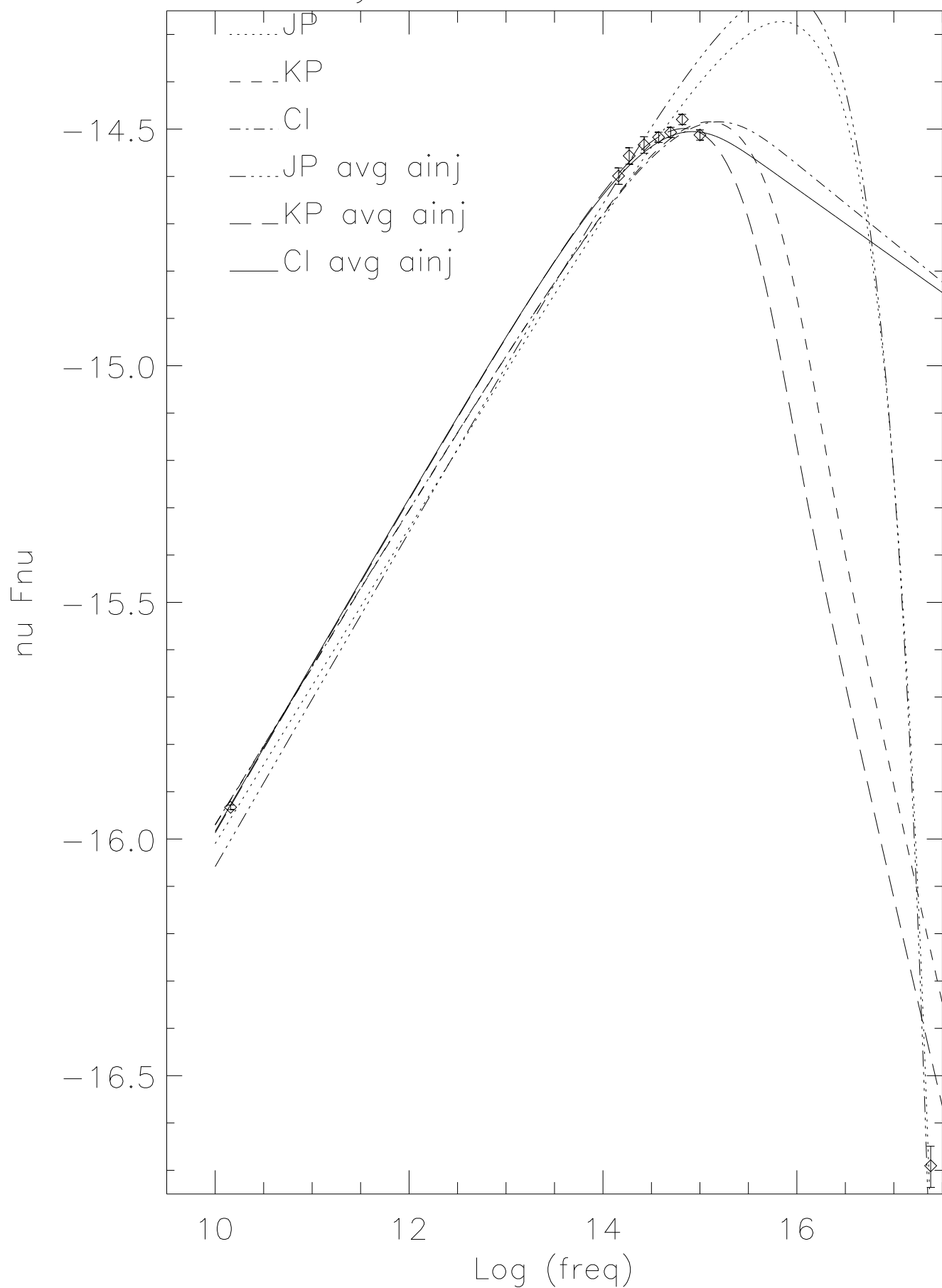
Synchrotron Models, D



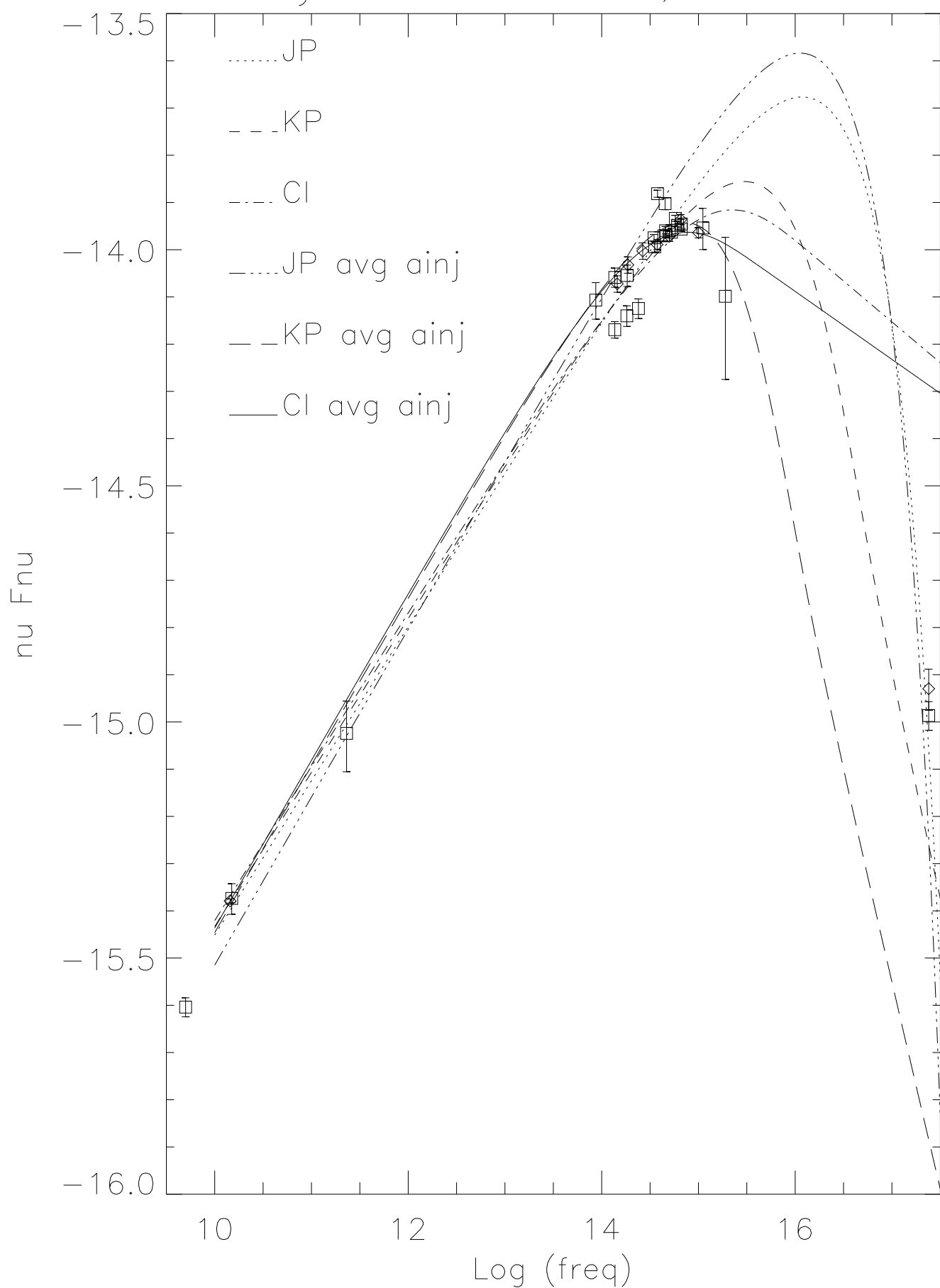
Synchrotron Models, A



Synchrotron Models, B



Synchrotron Models, A+B+C



Synchrotron Models, A+B+C

